Featured in Physics

Unconventional ^{67}Cu production using high-energy bremsstrahlung and cross section evaluation

M. Eslami,* D. G. Jenkins, and M. Bashkanov
School of Physics, Engineering and Technology, University of York, York YO10 5DD, United Kingdom

(Received 20 February 2025; revised 17 August 2025; accepted 15 September 2025; published 7 November 2025)

Background: The use of theranostic isotope pairs is an emerging field in contemporary medicine, yet their clinical availability is often constrained by production and supply chain challenges. Among them, ^{67}Cu has gained significant interest as the therapeutic counterpart in the ^{67}Cu / ^{64}Cu theranostic pair. Traditional production methods rely on reactor-based or charged-particle accelerator routes, both of which face limitations in scalability and isotopic purity.
Purpose: This work investigates the photonuclear production of ^{67}Cu via the ^{68}Zn(γ, p)^{67}Cu reaction, using high-energy bremsstrahlung photons from an electron accelerator. In addition to quantifying production yields and radionuclidic purity, the work provides spectrum-weighted average cross sections for multiple emission channels, serving as a test of reaction modeling under broad excitation conditions. The results inform both the optimization of ^{67}Cu production for theranostic applications and the improvement of nuclear reaction theory in an underexplored energy regime.
Method: Natural zinc targets were irradiated using bremsstrahlung photons from an 855 MeV electron beam at the Mainzer Mikrotron (MAMI). The photon energy spectrum was measured via tagging and extended beyond the tagged range using GEANT4 simulations. Reaction products were identified via gamma-ray spectroscopy, and spectrum-weighted average cross sections were derived. Theoretical cross sections were calculated using TALYS, incorporating giant dipole resonance and quasideuteron components of the photon absorption cross section. A model sensitivity analysis was performed to assess the influence of level density and photon strength function variations on the predicted cross sections.
Results: A production yield of 0.410(16) MBq μA^{-1}h^{-1}g^{-1} was measured for ^{67}Cu, with corresponding average cross sections determined from the bremsstrahlung spectrum. Yields and average cross sections were also measured for coproduced isotopes including ^{64}Cu, ^{61}Cu, ^{60}Cu, ^{69m}Zn, ^{65}Zn, ^{63}Zn, and ^{62}Zn. The relatively low production of nontarget isotopes indicates that the ^{68}Zn(γ, p)^{67}Cu reaction proceeds with favorable radionuclidic selectivity under the applied irradiation conditions. TALYS calculations showed good agreement with the (γ,p) channel, but neutron-emission and multi-particle channels were systematically overestimated. Model sensitivity points to assumptions in the photon strength function and level density, as well as the absence of explicit pion-resonance dynamics at high energies, as likely contributors to this behavior.
Conclusions: Photonuclear reactions provide a promising approach for high-purity ^{67}Cu production. Theoretical discrepancies highlight limitations in current reaction models, especially for (γ,xn) channels at high energy. Beyond this, the scalability of electron-driven methods, enabled by existing high-current infrastructure and compact low-energy linacs, offers flexibility for both centralized and decentralized isotope production. Continued development of accelerator technologies and nuclear models will be essential for expanding access to photonuclear-produced medical isotopes.

DOI: 10.1103/954z-cn34

I. INTRODUCTION

Recent advances in nuclear reaction studies, alongside developments in particle accelerator technologies, have significantly broadened the applications of radioisotopes over the past decades. These improvements are especially evident in nuclear medicine, where an increasing number of radionuclides, many previously considered rare or impractical, are moving closer to routine availability. A prominent example is the emergence of *theranostics*, where a combination of two radioisotope-containing drugs are employed simultaneously: one for molecular imaging for diagnosis and one for molecular targeted treatment for therapy. Indeed, this is an approach that many pharmaceutical companies are actively exploring with the hope that it may expedite the drug development process, mitigate risks, reduce overall costs, and enhance disease management [1].

The simplest approach to theranostics would be to employ two radioactive isotopes of the same element since they would naturally form the same chemical compounds [2]. Clearly,

*Contact author: mamad.eslami@alumni.york.ac.uk

TABLE I. Specific decay properties of copper isotopes, including the decay mode, mean beta and γ-ray energies, and their principal intensities.

Isotope	Half-life	Decay mode	$E_{\beta_{\text{mean}}}$ (keV)	I_β (%)	E_γ (keV)	I_γ (%)
^{60}Cu	23.7 m	β^+/EC	970	93	826.4	21.7
					1332.5	88.0
					1791.6	45.4
^{61}Cu	3.339 h	β^+/EC	500	61	282.956	12.7
					656.008	10.4
^{62}Cu	9.673 m	β^+/EC	1319	97.83	875.66	0.147
					1172.97	0.342
^{64}Cu	12.700 h	β^+/EC	278	17.49	1345.77	0.472
		β^-	191	38.5		
^{67}Cu	61.83 h	β^-	141	100	91.266	7.00
					93.311	16.10
					184.577	48.7
					300.219	0.797

that requires radioisotopes with favorable properties which reduces somewhat the field of potential candidates. Some of the radionuclide pairs considered as having high potential include: ^{86}Y / ^{90}Y, ^{124}I / ^{131}I, $^{43/44}$Sc / ^{47}Sc, and ^{64}Cu / ^{67}Cu. Here, we focus on the last example—an attractive one since the coordination chemistry of copper is well established [3], enabling copper to be linked to antibodies, proteins, and other biologically important molecules [4–7]. Moreover, copper offers several radioisotopes (see Table I) suitable for imaging (^{60}Cu, ^{61}Cu, ^{62}Cu, and ^{64}Cu) and therapy (^{64}Cu and ^{67}Cu). Research involving radiotheranostic isotopes is sometimes limited by their availability. The longest-lived radioisotope of copper, ^{67}Cu ($T_{\frac{1}{2}} = 61.83$ h), is an example of a promising radiotheranostic counterpart which suffers from lack of commercial interest because it usually requires a dedicated target system. ^{67}Cu can be combined with the same type of radiopharmaceuticals as ^{64}Cu ($T_{\frac{1}{2}} = 12.700$ h) or ^{61}Cu ($T_{\frac{1}{2}} = 3.3$ h), leading to an efficient theranostic pair [8] for performing low-dose PET dosimetric studies prior to therapy. Furthermore, the properties of its β^- (100%) decay ($E_{\text{mean}} =$ 141 keV) and associated 184 keV (48.7%), 93 keV (16.1%), and 91 keV (7.0%) gamma rays [9] (see Fig. 1) make ^{67}Cu suitable for single-photon emission computerized tomography (SPECT) imaging as well as for the treatment of diminutive tumors, typically measuring only a few millimeters.

In addition, ^{67}Cu offers benefits over conventional radioisotopes with longer half-lives, thereby mitigating the risk of excessive radiation exposure to the patient and people nearby. Another notable attribute of ^{67}Cu lies in its favorable biodistribution properties when employed as Cu^{2+}, as evidenced by recent studies consistently demonstrating their selective accumulation in cancerous tissues, indicating their potential as highly specific tumor markers [10]. These properties emphasize the enormous potential of ^{67}Cu for nuclear medicine.

It is important to note that, while the diagnostic counterpart, ^{64}Cu, has been extensively used in radiopharmaceuticals for a wide range of preclinical and clinical studies [4,11], the use of ^{67}Cu has been relatively limited but has shown promising results [12–15]. The main barrier to its broader preclinical and clinical application is its limited availability.

Currently, there is no reliable global supply of ^{67}Cu in clinical quantities. However, methods using particle accelerators have recently gained significant attention [16]. The primary production route at present involves the reaction ^{68}Zn(p,2p)^{67}Cu [17,18]. This approach requires 70–200 MeV proton beams, typically available in medium- to high-energy cyclotrons. By employing this route, small quantities of ^{67}Cu are occasionally produced at Brookhaven National Laboratories in the United States [18]. The main drawback of this route is a high ^{64}Cu / ^{67}Cu ratio in the final product. Other production routes based on lower-energy charged particle reactions are ^{70}Zn(p,α) ^{67}Cu [19,20], ^{70}Zn(d,αn)^{67}Cu [21], and ^{64}Ni(α,p)^{67}Cu [22,23]. Moreover, production routes based on reactions induced by accelerator-generated neutrons have been employed [24–27]. These routes have shown varying

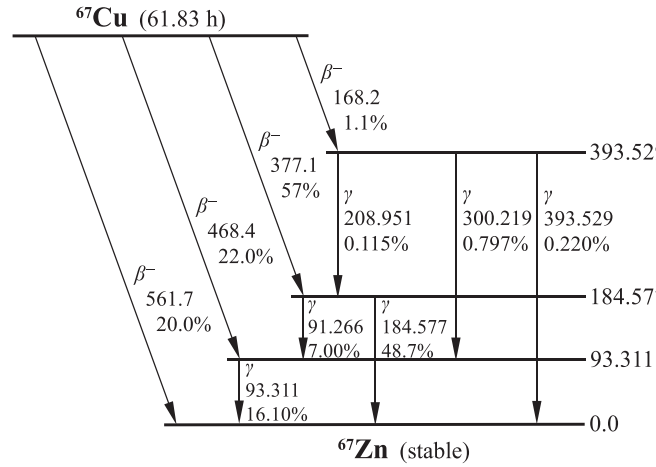

FIG. 1. Decay scheme for the β^- decay of ^{67}Cu into ^{67}Zn. Beta transitions are labeled with their respective endpoint energies in keV and their branching ratios in %. Subsequent gamma-ray transitions are labeled with their transition energies in keV and their branching ratios in %.

TABLE II. Potential production routes and their corresponding literature-reported yields for producing ^{67}Cu. The reported data have been standardized into the common unit of MBq $\mu A^{-1}h^{-1}g^{-1}$ at the end of bombardment (EOB). The standardized unit for the neutron-induced routes is MBq g^{-1}. Notably, only yields obtained through direct measurements with enough experimental details to extract the standardized yield are included, while those derived from excitation functions are excluded.

Reaction	Target	Enrichment [Purity] (%)	Mass (g)	Energy (MeV)	Current (μA)	Time (h)	^{67}Cu yield	$\frac{^{64}Cu}{^{67}Cu}$ ratio	Standardized yield (MBq $\mu A^{-1}h^{-1}g^{-1}$)	Reference
^{68}Zn(p,2p)	Zn	99.71	1.51	105	53.1	26.4	1.04 MBq $\mu A^{-1}h^{-1}g^{-1}$	16.1	1.04	[18]
	Zn	99.71	2.13	105	42.0	45.0	0.99 MBq $\mu A^{-1}h^{-1}g^{-1}$	6.9	0.99	[18]
	Zn	99.71	3.58	128	44.6	24.0	1.24 MBq $\mu A^{-1}h^{-1}g^{-1}$	8.2	1.24	[18]
	Zn	99.71	0.74	92	46.2	24.0	1.18 MBq $\mu A^{-1}h^{-1}g^{-1}$	10.8	1.18	[18]
	ZnO	99	3–3.7	70 → 50	3	6	117 MBq		1.7	[17]
^{nat}Zn(p,x)	Zn	[99.998]	5.75	67.7 → 52.8	71.4	28	1.4 MBq $\mu A^{-1}h^{-1}$	36.4	0.24	[33]
	ZnO	[99.999]	29	200			13.6 μCi $\mu A^{-1}h^{-1}$	6.2	0.017	[34]
	Zn		22	200			6.6 μCi $\mu A^{-1}h^{-1}$	9.5	0.011	[34]
	Zn		0.41–8.2	177.9–192.2	21–48.1	1–78	3.3 ± 0.2 μCi μA^{-1}/(mg cm^{-2} Zn)[a]	$10^{+2.3}_{-4.3}$	1.24 ± 0.07[a]	[35]
	ZnO	[99.9995]	2.86	128	42.3	24.0	0.26 MBq $\mu A^{-1}h^{-1}g^{-1}$	19.9	0.26	[18]
	ZnO	[99.9995]	2.90	105	45.6	66.3	0.14 MBq $\mu A^{-1}h^{-1}g^{-1}$	15.6	0.14	[18]
^{70}Zn(p,α)	Zn	97.5	0.130	17	60	4–6	1 MBq $\mu A^{-1}h^{-1}$	< 0.003	7.69	[36]
	Zn	70.2	0.100	20 → 17	10	10	10 MBq	1	1	[20]
	Zn	70.2	0.100	16 → 12.5	20	5	14 MBq	0.5	1.4	[20]
	Zn or ZnO	99.72	0.00169–0.010	18.8 → 18.5	2–5.7	0.33–1	8.88 kBq $mg^{-1}h^{-1}mA^{-1}$		0.00888	[19]
^{64}Ni(α,p)	Ni	99.07	0.092 ± 0.004	36 → 0	15	7	55 ± 10 MBq	0.259	5.69 ± 1.03	[22]
^{68}Zn(γ, p)	Zn		55.5	40	455	53.5	62.9 GBq		0.04655	[37]
	ZnO	98.97	0.025	30	175	0.5	0.41 μCi $\mu A^{-1}h^{-1}$/(100 mg ZnO)	0.0027	0.1517	[31]
	ZnO	98.97	0.025	40	175	0.5	0.774 μCi $\mu A^{-1}h^{-1}$/(100 mg ZnO)	0.0052	0.2863	[31]
	ZnO	98.97	0.025	50	175	0.5	0.922 μCi $\mu A^{-1}h^{-1}$/(100 mg ZnO)	0.0093	0.3411	[31]
	ZnO	98.97	0.025	60	175	0.5	1.29 μCi $\mu A^{-1}h^{-1}$/(100 mg ZnO)	0.0067	0.4773	[31]
^{nat}Zn(γ,x)	Zn		0.2, 0.21, 0.4	15	58	0.75	2.07 ± 0.35 kBq g^{-1}[b]		$(4.75 \pm 0.80) \times 10^{-5}$	[28]
	Zn			30			1.02 ± 0.04 MBq $g^{-1}kW^{-1}h^{-1}$		$(3.40 \pm 0.13) \times 10^{-5}$	[29]
	Zn		100	35	50	48	5 mCi/(100 g Zn)[c]	0.01[c]	0.00135	[38]
	ZnO	[99.9]	1.19	40		1	4.75 μCi $\mu A^{-1}h^{-1}g^{-1}$		0.176	[39]
	ZnO	[99.9]	2.09	30		1	2.04 μCi $\mu A^{-1}h^{-1}g^{-1}$		0.0755	[39]
	Zn		40	30.0 ± 2.1	1000	1	7.1 ± 2.1 MBq g^{-1}		0.0071 ± 0.0021	[30]
	Zn		40	35.0 ± 2.9	1000	1	14.4 ± 2.9 MBq g^{-1}		0.014 ± 0.0029	[30]
	Zn		40	38.0 ± 3.4	1000	1	17.0 ± 3.4 MBq g^{-1}		0.017 ± 0.0034	[30]
	Zn			36	260	0.16–2.25	0.068 mCi $g^{-1}h^{-1}$/(100 μA)		0.02516	[40]
	Zn			30	166.6	5.25–10	0.05 mCi $g^{-1}h^{-1}$/(5 kW)		0.0111	[41]
^{67}Zn(n,p)	ZnO	93.2		Mixed[d]	Mixed[e]	Variable[f]	90.2 ± 9.5 μCi mg^{-1}		3337 ± 351[g]	[35]
^{nat}Zn(n,x)	Zn		3.3	14.1	200[h]	0.33	1.51 ± 0.26 Bq g^{-1}	$115.8^{+38.0}_{-27.6}$	$(1.51 \pm 0.26) \times 10^{-6}$[g]	[28]
	Zn	[99.99]	55.401	40[i]	4.9[j]	3	5.49 MBq	72	0.099[g]	[42]

[a]Average of runs 1–9.
[b]Averaged over three measurements with three different masses.
[c]Reported for 50 hours after EOB.
[d]Reactor core energy spectrum.
[e]$(1.95 \times 10^{14}\ n_{\text{thermal}}\ s^{-1}cm^{-2}) + (3.0 \times 10^{14}\ n_{\text{fast}}\ s^{-1}cm^{-2})$.
[f]Few hours to several days.
[g]In MBq g^{-1}.
[h]D^+ current for DT reaction.
[i]Deuteron beam energy for ^{9}Be(d,n) reaction.
[j]Deuteron beam current for ^{9}Be(d,n) reaction.

levels of success in terms of yield, scalability, and radionuclidic purity. An alternative production method using photonuclear reactions, driven by bremsstrahlung photons from high-intensity electron accelerators, has attracted growing attention [28–31]. Table II summarizes the major production routes investigated for ^{67}Cu, including photonuclear and nonphotonuclear methods, alongside their reported production yields. For ease of comparison, we have standardized the reported data into common units corresponding to MBq $\mu A^{-1}h^{-1}g^{-1}$ at the end of bombardment (EOB).

In addition to offering a nonproliferative route, the photonuclear approach enables the simultaneous production of multiple medically relevant radionuclides within a single irradiation cycle, potentially reducing both operational

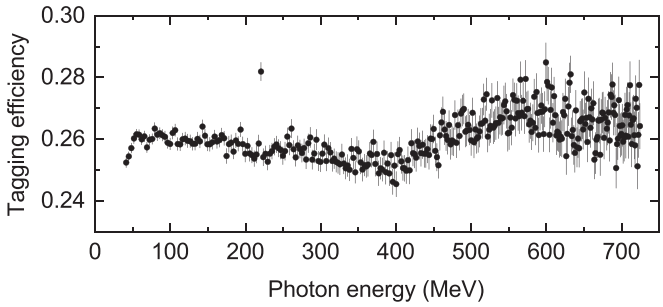

FIG. 2. Measured tagging efficiency $\epsilon_{\text{tag}}(E_\gamma)$ as a function of photon energy during the experiment. The tagging efficiency remains nearly constant at ≈ 0.25–0.28 across the tagged photon energy range, consistent with expectations for an unpolarized bremsstrahlung beam from a thin amorphous radiator.

complexity and cost. However, the feasibility of such an approach critically depends on the availability of accurate and comprehensive nuclear data, particularly cross sections for competing reaction channels, across a broad energy range extending well beyond the giant dipole resonance (GDR) region.

Photon beams in the intermediate energy range (10–200 MeV) remain relatively scarce and are typically available at large-scale facilities dedicated to hadron physics research, such as the Thomas Jefferson National Accelerator Facility (JLab), the Mainzer Mikrotron (MAMI), the Electron Stretcher Accelerator (ELSA) at the University of Bonn, and the Super Photon Ring-8 GeV (SPring-8) in Japan. These facilities often operate under heavy scientific demand, making it difficult to allocate dedicated beamtime for systematic photonuclear cross section measurements. However, due to the small electromagnetic coupling, bremsstrahlung photon beams can traverse primary targets with relatively low attenuation. This enables the possibility of parasitic measurements downstream or near beam dumps, where photons that are not absorbed in the main experiment may still be used to irradiate secondary targets.

The objective of the present study was to explore alternative methods of producing ^{67}Cu that offer increased yield and radionuclidic purity, thus ensuring a more secure supply of this radionuclide. Specifically, we investigated photonuclear production of ^{67}Cu through the ^{68}Zn(γ,p) reaction using a bremsstrahlung photon beam generated parasitically at a high-energy electron accelerator facility. This setup demonstrates that photonuclear measurements can be performed opportunistically, using the residual photon flux beyond a primary target without requiring dedicated beam time. Beyond the applied motivation, the study also examines the broader photonuclear reaction landscape on natural zinc, characterizing the coproduction of several other radionuclides. By comparing experimental yields and spectrum-weighted cross sections with theoretical predictions from TALYS [32], we test the reliability of statistical reaction models across multiple reaction channels. A systematic model sensitivity analysis is performed to evaluate how variations in nuclear inputs affect the accuracy of predicted cross sections, particularly for neutron-emission channels. This approach enables both the practical assessment of ^{67}Cu production and a broader evaluation of reaction theory in the high-excitation regime relevant to bremsstrahlung activation. Accordingly, this work addresses the following questions: (a) What is the maximum quantity of ^{67}Cu that can be produced through the $^{\text{nat}/68}$Zn(γ,p) reactions and what are the optimal irradiation parameters? (b) What are the levels and origins of various byproducts produced in the process? (c) How accurately do theoretical models predict cross sections across different channels and what are the dominant sources of uncertainty? (d) What practical considerations influence the feasibility and scalability of this production route, including compatibility with existing accelerator infrastructure?

II. MATERIALS AND METHODS

A. Experimental procedure

The experiment was carried out parasitically using bremsstrahlung photons generated by an 855 MeV electron beam from the MAMI [43] incident on a thin Møller radiator (VACOFLUX 50 alloy: 49% Co, 49% Fe, 2% V) with a thickness of 10 μm, located in the A2 Collaboration hall [44]. The electron beam current during the experiment was maintained at 8 nA.

The photon energy distribution was characterized using the upgraded Glasgow-Mainz photon tagging spectrometer [45]. This technique involves detecting post-bremsstrahlung electrons whose deflection in a dipole magnet is directly related to the photon energy emitted during bremsstrahlung. By recording the electron position in a segmented focal-plane detector array, the corresponding photon energy can be precisely inferred.

Typically, photon tagging is employed for selecting photons of known energies to study exclusive photonuclear reactions. In this experiment, however, the tagging spectrometer primarily served to characterize the photon energy distribution (differential photon rate). Although the final cross section results were obtained by integrating over the entire photon energy spectrum, precise knowledge of the differential photon rate was essential for validating the experimental bremsstrahlung spectrum, normalizing simulations, and enabling reliable extrapolation into regions where direct measurement was not feasible.

To ensure the photon beam remained fully contained within the target diameter, the bremsstrahlung photons were collimated through a lead collimator measuring 20 cm in length and 3 mm in diameter. At relativistic electron energies, bremsstrahlung emission is strongly forward peaked with an angular spread approximately given by $\theta \approx 1/\gamma$, where γ is the Lorentz factor. Thus, the narrow collimator aperture excluded photons emitted at larger angles, maintaining a well-defined beam profile at the target.

The fraction of tagged photons actually passing through the collimator and reaching the target, known as the tagging efficiency $\epsilon_{\text{tag}}(E_\gamma)$, was measured daily using a dedicated lead-glass Cherenkov detector placed downstream of the collimator. The detector consists of a 20 cm thick lead glass block (approximately 16 radiation lengths), providing nearly 100% photon detection efficiency. Incident photons produce

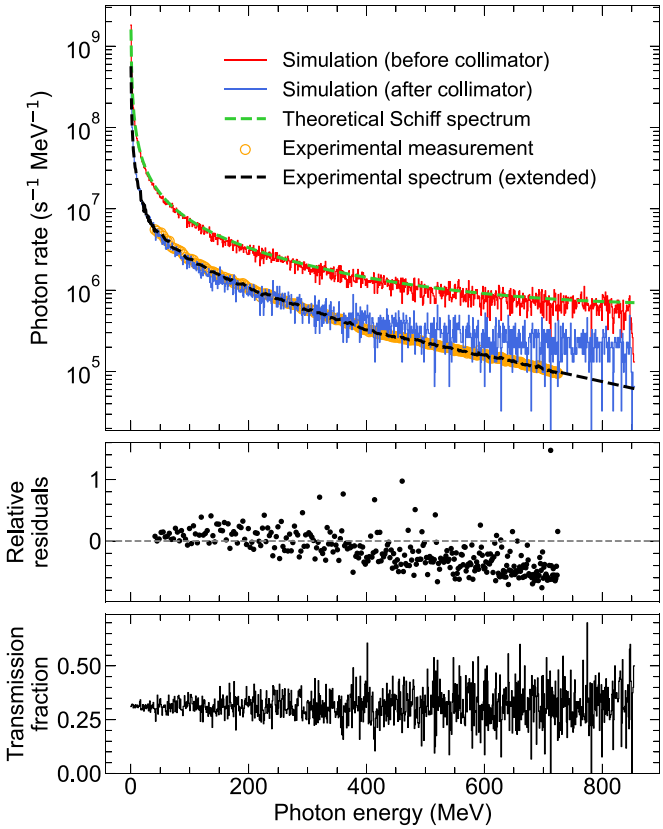

FIG. 3. Comparison of measured and simulated bremsstrahlung spectra. *Top:* Photon rate spectra (1 MeV bins) as a function of photon energy. Orange open circles represent the experimental data (41.3–724.4 MeV), while the dashed black line shows the extended spectrum, constructed by stitching the simulated after-collimation spectrum outside the measured range. The simulated spectra before and after collimation, along with the analytical Schiff distribution, are also shown for reference. *Middle:* Relative residuals between the experimental and simulated after-collimation spectra, calculated as (Expt − Sim)/Sim. The residuals demonstrate good agreement and validate the use of the simulation for spectrum extrapolation. *Bottom:* Simulated energy-dependent photon transmission fraction through the 3 mm collimator, showing nearly constant behavior across the photon energy range.

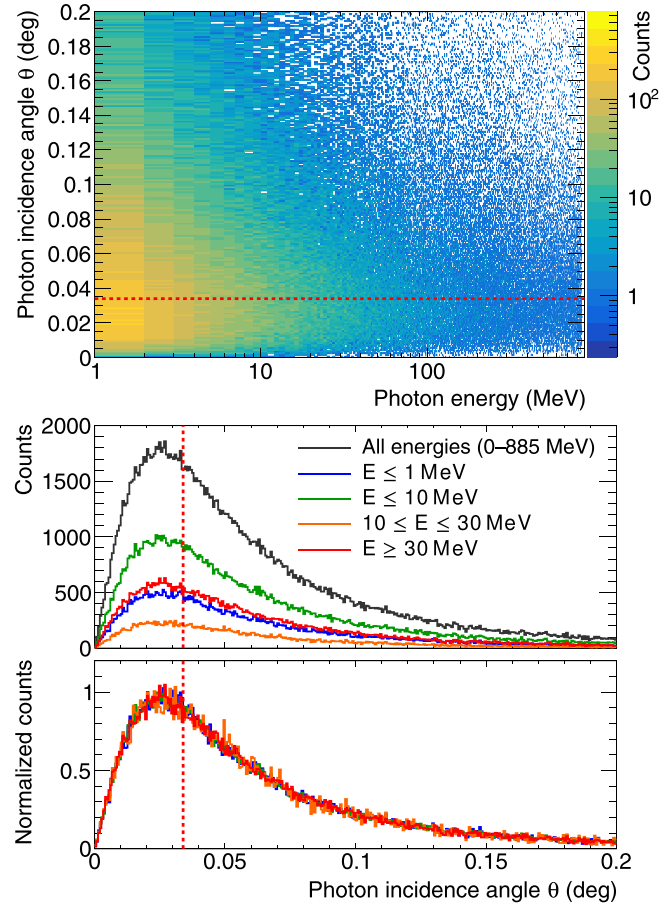

FIG. 4. Angular distribution of bremsstrahlung photons at the collimator entrance. *Top:* 2D heatmap of photon energy versus incidence angle at the pre-collimator scoring plane. The red dashed line indicates the acceptance angle for the 3 mm collimator (0.034°). *Middle:* Projected incidence angle distributions (raw counts) for different photon energy ranges. *Bottom:* Same projections after normalization to an area of 100 for comparison. The nearly perfect overlap of the normalized angular distributions demonstrates that the angular spread is independent of photon energy.

electromagnetic showers of electron-positron pairs, generating Cherenkov radiation collected by a photomultiplier tube (PMT). Tagging efficiency measurements were conducted at a reduced beam intensity (a few kHz) to prevent PMT saturation, and background measurements without beam were performed before and after each tagging run. The resulting tagging efficiency, shown in Fig. 2, was nearly constant (≈0.25–0.28) across the measured energy range. This energy independence arises from the use of an ultrathin (10 μm) amorphous radiator, as well as the minimal photon angular spread at high electron energies.

During regular production runs, high-intensity beam conditions required the removal of the high-energy electron detectors from the tagger focal plane to avoid detector damage. Consequently, no experimental photon data were collected below 41.3 MeV or above 724.4 MeV. To reconstruct the complete bremsstrahlung photon distribution, a detailed GEANT4 [46] simulation incorporating the actual experimental geometry (radiator, collimator, beam transport) was performed. The bremsstrahlung photon production and transport were modeled using the Livermore electromagnetic physics models, which are optimized for photon and electron interactions from a few hundred eV up to 1 GeV. These models provide precise treatment of the photoelectric effect, Compton scattering, bremsstrahlung, and pair production processes through the use of evaluated data libraries such as EEDL [47]. The angular distribution of the emitted photons was sampled using the generator `G4ModifiedTsai` [48], which implements a simplified form [49] of Tsai's differential cross sections, based on the original formulation by Tsai [50], to reproduce photon emission angles across the relevant energy range. Comparative simulations using the GEANT4 Standard Electromagnetic and Penelope [51] physics lists showed no significant differences in the resulting bremsstrahlung spectra.

Based on this agreement, and the known strengths of the Livermore models in the photonuclear energy regime of interest, the Livermore physics list was adopted for the simulations.

The measured differential photon rate between 41.3 and 724.4 MeV was combined with the simulated spectrum at lower (head) and higher (tail) energies, as illustrated in Fig. 3 (top panel). No additional scaling was applied; the simulated after-collimation spectrum was directly normalized to match experimental data within the tagged region. The simulation's reliability outside the tagged region was further cross-checked by comparing the simulated spectrum to the analytical Schiff bremsstrahlung distribution, which describes photon emission from thin targets in the complete screening limit. The excellent agreement between the simulation and the Schiff distribution, also shown in Fig. 3 (top panel), confirms the physical consistency of the extrapolated low-energy and high-energy tails. The middle panel of Fig. 3 shows the relative residuals between the experimental and simulated after-collimation photon spectra, expressed as (Expt − Sim)/Sim. The residuals are centered around zero across the tagged energy range (41.3–300 MeV), with no significant systematic trends observed. This good agreement between experiment and simulation supports the reliability of the simulation-based extrapolation into the unmeasured low- and high-energy regions. Deviations observed at higher photon energies are of reduced concern, as the photonuclear cross sections vanish in that region and thus contribute minimally to the overall production. A detailed evaluation of the residuals and the associated uncertainty introduced by the spectrum extension is discussed separately in the uncertainty analysis (Sec. II C).

Further justification for the use of simulation data in extending the photon spectrum is provided by analyzing collimator transmission (bottom panel of Fig. 3) and photon angular distributions (Fig. 4). Collimator transmission remains constant at approximately 31% across the entire photon energy range, confirming minimal spectral distortion by the collimator. Additionally, the angular distribution analysis shown in Fig. 4 reveals energy-independent photon angular spread. The two-dimensional (2D) heatmap (top panel) and angular projections (middle and bottom panels) indicate that photons remain narrowly forward peaked due to minimal electron multiple scattering in the ultrathin radiator (only a fraction of its 1.69 cm radiation length). The normalized angular distributions overlap almost perfectly across energy ranges, reinforcing the reliability of the simulated photon spectrum extension.

Together, the spectral, angular, and transmission analyses support the reliability of the extended photon spectrum and its use for normalizing the photon energy distribution in cross section calculations.

Further details about the tagging spectrometer, the lead-glass detector performance, and tagging efficiency measurement methods are available in Ref. [45].

During the irradiation process, continuous monitoring of the beam position was maintained using a photon camera. This was done to guarantee uninterrupted coverage of the target area without any deviation, ensuring a consistent and stable beam spot throughout the entire irradiation duration.

TABLE III. Isotopic composition of natural zinc [54].

Isotope	^{64}Zn	^{66}Zn	^{67}Zn	^{68}Zn	^{70}Zn
Natural abundance (%)	49.17	27.73	4.04	18.44	0.61

Furthermore, the precision of the beam spot was validated using a Gafchromic™ film, which confirmed the precise alignment of the resulting beam spot.

Various sets of 25 mm×25 mm natural zinc foils (Goodfellow Cambridge Limited, UK [52]) were positioned behind the collimator and exposed to irradiation durations ranging from several minutes to a few days. The foil thicknesses varied from 1 to 7 mm. The isotopic composition of natural zinc can be found in Table III. Residual nuclei were identified through their half-lives and characteristic gamma lines using a high purity germanium (HPGe) detector. The detector efficiency was determined by measuring a standard mixed gamma source (Eckert & Ziegler; serial No. BC-7896 [53]), and the resulting fitted efficiency curve is shown in Fig. 5. The following fit function was used:

$$\epsilon = \frac{1}{E_\gamma} \sum_{i=1}^{n} C_i \ln E_\gamma^i, \tag{1}$$

where E_γ is energy of the γ ray and C is fitting function parameter. The fitting order, represented as n, can be adjusted to achieve the best fit; in this scenario, n was set to 6.

The radioactivity of ^{67}Cu at EOB, along with the EOB activities of other products, was determined by quantifying the photopeak counts of the principal γ lines using the following equation:

$$A = \frac{C\,\lambda}{1 - e^{-\lambda t_{m_r}}} \frac{1}{e^{-\lambda t_c}} \frac{t_{m_r}}{t_{m_l}} \frac{f_a}{\epsilon\, I_\gamma}, \tag{2}$$

where C is the counts under the photo-peak, λ is the decay constant of the product, t_{m_r} is the real measurement time, t_{m_l} is the live measurement time, t_c is the cooling time, ϵ is the efficiency of the HPGe detector for the γ-ray energy considered, I_γ is the intensity of the γ ray of interest, and f_a is the attenuation factor to correct for the gamma self-absorption in the target, given by the following equation:

$$f_a = \frac{(\mu/\rho)\rho d}{1 - e^{-(\mu/\rho)\rho d}}, \tag{3}$$

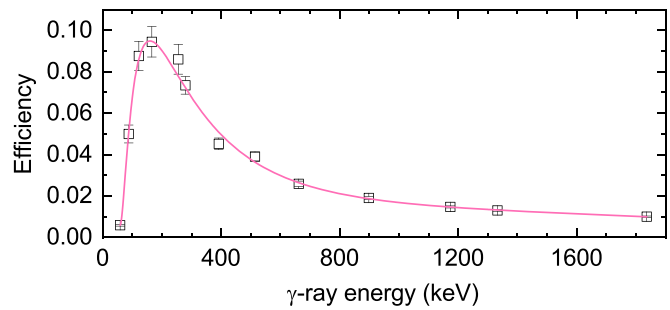

FIG. 5. Efficiency calibration of the HPGe at its end-cap using a mixed source. The solid line is a fit using the Eq. (1)

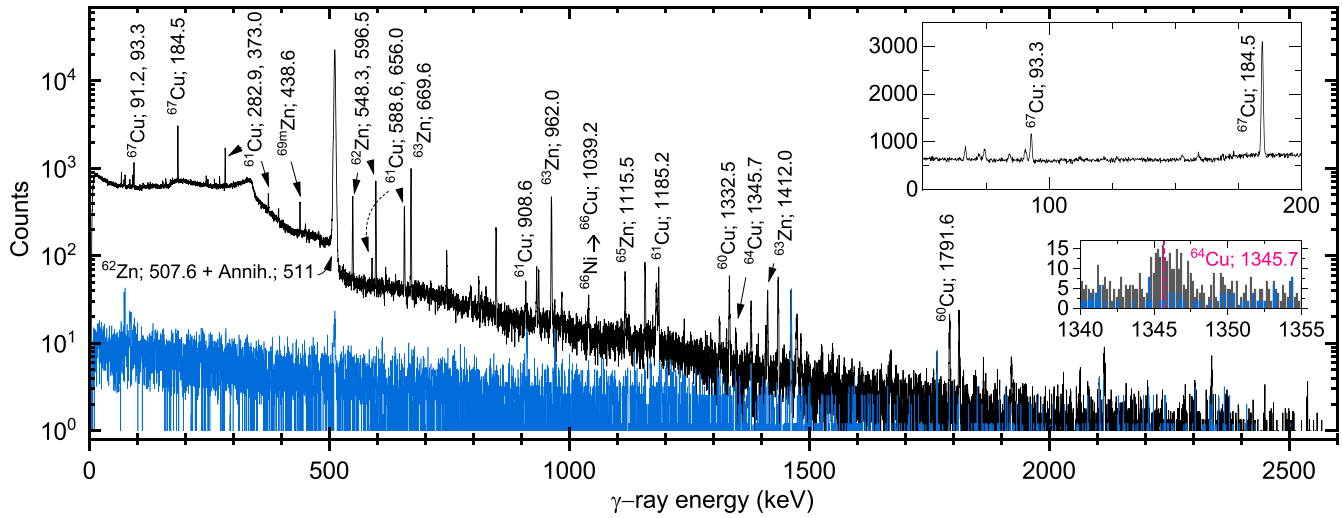

FIG. 6. Spectrum of induced activity from an irradiated natural zinc target, recorded 12 min after EOB for 2 h. The main radionuclides are marked by their name and energy in keV. The blue spectrum shows the background recorded for the same duration of 2 h. The upper-right inset highlights the peaks at 184.5 and 93.3 keV, used for determining the activity of ^{67}Cu. The lower-right inset shows a magnified view of the weak ^{64}Cu peak at 1345.7 keV, which is distinguishable above the local background.

where (μ/ρ) is the mass attenuation coefficient for a specific γ-ray energy, ρ is the mass density of the target, and d is the target thickness. The mass attenuation coefficients were taken from the NIST database [55]. Figure 6 shows the background-subtracted gamma-ray spectrum of one of the irradiated $^{\text{nat}}$Zn via bremsstrahlung photons. The spectrum was recorded 12 min after the EOB for 2 h. The background radiation was recorded for the same duration of 2 h.

B. Photonuclear cross section calculations

The photoabsorption cross section, $\sigma_{\text{abs}}(E_\gamma)$, in mb, is calculated using the quasideuteron (QD) approximation [56], as implemented in the TALYS code, and expressed as

$$\sigma_{\text{abs}}(E_\gamma) = \sigma_{\text{GDR}}(E_\gamma) + \sigma_{qd}(E_\gamma), \tag{4}$$

where E_γ is the incident photon energy in MeV. The GDR component, $\sigma_{\text{GDR}}(E_\gamma)$, is given by a Lorentzian function

$$\sigma_{\text{GDR}}(E_\gamma) = \sum_i \sigma_{E1} \frac{(E_\gamma \Gamma_{E1,i})^2}{\left(E_\gamma^2 - E_{E1,i}^2\right)^2 + E_\gamma^2 \Gamma_{E1,i}^2}, \tag{5}$$

where the sum over i is taken over the number of the parts into which the GDR is split. The GDR component is related to the photon strength function (PSF) by

$$f_{Xl}(E_\gamma) = K_{Xl} \frac{\sigma_{Xl}}{E_\gamma^{2l-1}}, \tag{6}$$

where

$$K_{Xl} = \frac{1}{(2l-1)\pi^2\hbar^2c^2}. \tag{7}$$

Here X represents either electric E or magnetic M radiation, and l is the radiation multipolarity. σ_{Xl} denotes the experimental photoabsorption cross section over all spins and parities. There are various phenomenological and microscopic models for the PSF. The phenomenological models implemented in TALYS are generally parameterized in terms of Lorentzian forms with GR parameters σ_{Xl}, E_{Xl}, Γ_{Xl} being strength, energy, and width of the GR, respectively. For all Xl transitions, systematic formulas [57] for the resonance parameters are used. The QD component σ_{qd} is given by [58]

$$\sigma_{qd}(E_\gamma) = L\frac{NZ}{A}\sigma_d(E_\gamma)f(E_\gamma), \tag{8}$$

where $L = 6.5$ is the Levinger parameter quantifying the excess of high momenta in the QD relative to that in the free deuteron, NZ is the number of neutron-proton pairs in the nucleus, A is the mass number, $\sigma_d(E_\gamma)$ is the free deuteron photodisintegration cross section in mb, and $f(E_\gamma)$ is the Pauli blocking function. The deuteron photodisintegration cross section is parametrized as [59]

$$\sigma_d(E_\gamma) = 61.2\frac{(E_\gamma - 2.224)^{3/2}}{E_\gamma^3}\ \text{mb}, \tag{9}$$

where E_γ is in MeV. The Pauli-blocking function $f(E_\gamma)$ accounts for those excitations of neutron-proton pairs that cannot occur since the Pauli exclusion principle allows only final particle states which lie above the Fermi level. This effect is particularly important for low photon energies. It is

approximated by the polynomial expressions [56,60]

$$f(E_\gamma) = \begin{cases} 8.3714\times10^{-2} - 9.8343\times10^{-3}E_\gamma + 4.1212\times10^{-4}E_\gamma^2 - 3.4762\times10^{-6}E_\gamma^3 & \\ +9.3537\times10^{-9}E_\gamma^4, & 20 < E_\gamma < 140 \text{ MeV}, \\ e^{-73.3/E_\gamma}, & E_\gamma < 20 \text{ MeV}, \\ e^{-24.2348/E_\gamma}, & E_\gamma > 140 \text{ MeV}. \end{cases} \tag{10}$$

The theoretical average cross section $\langle\sigma\rangle_{\text{theo}}$ is calculated by weighting the modeled photoabsorption cross section $\sigma_{\text{abs}}(E)$ with the measured differential photon rate $\phi(E)$ according to

$$\langle\sigma\rangle_{\text{theo}} = \frac{\int_{E_{\text{th}}}^{E_{\text{end}}} \sigma_{\text{abs}}(E)\,\phi(E)dE}{\int_{E_{\text{th}}}^{E_{\text{end}}} \phi(E)dE}, \tag{11}$$

where E_{th} and E_{end} denote the reaction threshold energy and the bremsstrahlung endpoint energy, respectively. The experimental average cross section $\langle\sigma\rangle_{\text{expt}}$ is determined from the measured EOB activity A, the integrated photon rate Φ_{expt}, and the target areal density n, using

$$\langle\sigma\rangle_{\text{expt}} = \frac{A}{\Phi_{\text{expt}}\, n\,(1 - e^{-\lambda t_i})}, \tag{12}$$

where t_i is the irradiation time and the areal density is given by $n = \frac{N_{\text{A}}\,\rho\,d}{M}$, with N_{A} as Avogadro's number and M the molar mass of the target. In this work, the integrated photon rate Φ_{expt} corresponds to the same quantity as the denominator of Eq. (11), obtained from the extended experimental photon spectrum.

Following the experimental measurements and cross section calculations, the associated uncertainties were systematically evaluated, as detailed below.

C. Uncertainty analysis

The experimental uncertainty was evaluated by identifying and quantifying the main sources of error contributing to the determination of the EOB activity, the calculated yields, and the final cross sections.

The activity A of each isotope was determined by fitting the net γ-ray peak areas from HPGe spectra. When multiple γ lines were available, weighted averaging was performed, and uncertainties were propagated accordingly. Standard error propagation formulas were applied, taking into account counting statistics, detector efficiency uncertainties, and nuclear data uncertainties.

The yield calculation accounted for uncertainties from the measured activity and from the normalization of the photon energy distribution, which itself involved the measured tagging efficiency, spectrum extension, and focal-plane detector stability.

The uncertainty associated with the extension of the photon spectrum into unmeasured regions was evaluated by analyzing the relative residuals between the experimentally measured and simulated after-collimation photon spectra. The standard deviation of the residuals, defined as (Expt − Sim)/Sim, was calculated separately over different photon energy intervals. Between 41.3 and 100 MeV, the standard deviation was found to be 7.4%. In the 100–300 MeV region it increased to 17.1%, and above 300 MeV it reached 28.9%. Since the photonuclear cross sections peak at relatively low photon energies, the convolution is primarily influenced by the low-energy portion of the bremsstrahlung spectrum, where the intensity is highest. Nevertheless, contributions from higher-energy photons are not entirely negligible, especially in channels with extended excitation functions. To avoid overstating the impact of less dominant regions while ensuring a conservative estimate, a 7.5% systematic uncertainty to the spectrum normalization was assigned based on the standard deviation of residuals between simulation and measurement in the 41.3–100 MeV interval. Although the extrapolated region below 41.3 MeV lies beneath the tagging threshold and cannot be directly validated, the bremsstrahlung spectrum in this range is shaped primarily by well-understood primary emission processes and is less sensitive to beamline geometry or secondary interactions. The smooth spectral increase toward lower energies further supports the stability of this extrapolation. Moreover, the good agreement observed in the adjacent energy intervals provides confidence that no significant distortions are introduced near the lower boundary. Any substantial deviation in the simulation would likely manifest as a discontinuity at this edge, which is not observed. We therefore consider the 7.5% uncertainty to remain appropriate across the full low-energy range relevant to the folding calculation.

The final uncertainty on the experimental cross section $\langle\sigma\rangle_{\text{expt}}$ was obtained by propagating the uncertainties associated with the activity measurement, the normalization of the incident photon spectrum, and the target areal density. All uncertainties were treated as independent and combined in quadrature. A summary of the main uncertainty sources and their typical magnitudes is provided in Table IV. A total uncertainty range of 13–20% is obtained by quadrature addition of the listed contributions, depending on statistical and systematic factors. It is noted that this total uncertainty applies to individual cross section measurements. When multiple measurements are available for a given nuclide, weighted averaging leads to smaller combined uncertainties due to statistical reduction. Therefore, the uncertainties reported for yield and average cross sections in Sec. III may be lower than the 13–20% range cited here.

III. RESULTS AND DISCUSSION

As shown in Fig. 6, following the irradiation of $^{\text{nat}}$Zn using bremsstrahlung photons, coproduction of the radionuclides ^{64}Cu, ^{61}Cu, ^{60}Cu, ^{69m}Zn, ^{65}Zn, ^{63}Zn, and ^{62}Zn was observed. Therefore, the isotopic composition of the target

TABLE IV. Summary of uncertainty contributions to the experimental activity, photon spectrum normalization, and cross section.

Source	Typical uncertainty (%)	Comment
Peak area fitting (counting statistics)	4–10	Depends on counting statistics
HPGe efficiency (curve fit + calibration)	4–10	Combined calibration source and fit uncertainty
Nuclear data (branching ratios, half-lives)	<2	From evaluated nuclear data libraries
Target areal density	10	From target thickness and density measurements
Bremsstrahlung spectrum normalization	7.5	Includes tagging efficiency and focal-plane monitor
Theoretical spectrum-weighted cross section[a]	7.5	From experimental photon spectrum used in folding
Typical total (quadrature sum)	13–20	Reaction and energy dependent

[a]Theoretical spectrum-weighted cross sections are folded with the experimentally normalized bremsstrahlung spectrum; hence they inherit the 7.5% normalization uncertainty.

material becomes a critical factor for optimizing both yield and radionuclidic purity in the production of ^{67}Cu. The use of an enriched ^{68}Zn target is therefore preferred to suppress undesirable reaction channels. However, stable non-isotopic or long-lived impurities, such as ^{65}Zn, can be removed through chemical separation, while short-lived impurities typically decay during processing and transport, given the relatively long half-life of the main product, ^{67}Cu.

Among these coproduced radionuclides, ^{64}Cu is of particular relevance, not only because of its theranostic interest but also due to its impact on the overall ^{64}Cu / ^{67}Cu ratio. Although ^{64}Cu is produced with a considerable yield in the irradiation of natural zinc, its most prominent γ ray at 1345.7 keV has a very low emission probability of 0.472% and lies in an energy region where the absolute detection efficiency of the HPGe detector is markedly reduced. As a consequence, the corresponding peak in the spectrum appears weak. Nevertheless, when evaluated according to the rigorous formalism of Currie [61], the signal clearly surpasses the statistical requirements for detection. The critical level is defined as

$$L_c = k_\alpha \sqrt{B},$$

where k_α is the coverage factor corresponding to the chosen confidence level, typically 1.645 for 95% confidence, and B is the number of background counts under the region of interest. The detection limit is then expressed as

$$L_d = 2.71 + 4.65\sqrt{B},$$

which represents the minimum net signal required to claim detection at the same confidence level. In our case, the net peak area exceeds both L_c and L_d, demonstrating conclusively that the 1345.7 keV line of ^{64}Cu is statistically detectable. This is further substantiated by the magnified inset in Fig. 6, where the peak, although shallow, emerges distinctly above the local background. The 511 keV annihilation line was deliberately excluded from the analysis, since it receives unavoidable contributions from positron-emitting zinc isotopes such as ^{65}Zn, ^{63}Zn, and ^{62}Zn, and, even after chemical separation of zinc, annihilation photons from co-produced copper isotopes such as ^{61}Cu and ^{60}Cu would persist. Only when using an enriched ^{68}Zn target with the reaction threshold carefully controlled to suppress these competing copper channels could the 511 keV line potentially become an unambiguous signature of ^{64}Cu. The observed strength of this peak and its underlying reaction mechanisms are examined in detail in the subsequent analysis.

A production yield of 0.410(16) MBq μA^{-1}h^{-1}g^{-1} was measured for ^{67}Cu. Figure 7 shows that a significant portion of this production occurs within the GDR region, between 10 and 30 MeV, where the photoabsorption cross section is high. A small contribution is also expected from ^{70}Zn(γ,x) reactions; however, this is negligible due to the isotope's low natural abundance (0.61%), its high threshold energy, where the bremsstrahlung spectrum is reduced, and its generally lower cross section compared to the ^{68}Zn(γ, p) ^{67}Cu reaction.

Figure 8 presents the theoretical photonuclear reaction cross sections for additional radionuclides produced alongside ^{67}Cu. The energy windows shown highlight the regions of significant cross section, and their relative contributions in a natural zinc target are evident. The figure illustrates that, in addition to the desired ^{67}Cu, a number of copper and zinc radionuclides are unavoidably produced, each through distinct reaction channels. Among these, ^{64}Cu is of particular importance because it cannot be easily separated from ^{67}Cu and its relatively long half-life prevents decay-based removal without significant loss of ^{67}Cu. In contrast, other byproducts are

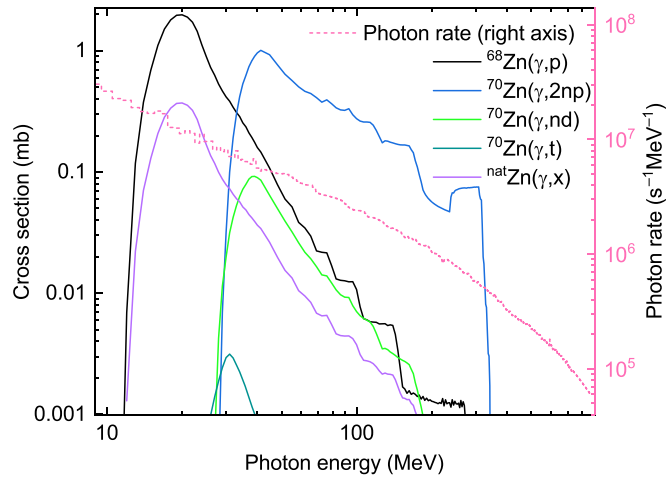

FIG. 7. Theoretical cross sections of ^{x}Zn(γ, x) ^{67}Cu reactions calculated by Eq. (4) in TALYS with default parameters (left axis), alongside the measured photon rate spectrum (right axis). A convolution of the cross section and photon rate yields the theoretical average cross section according to Eq. (11).

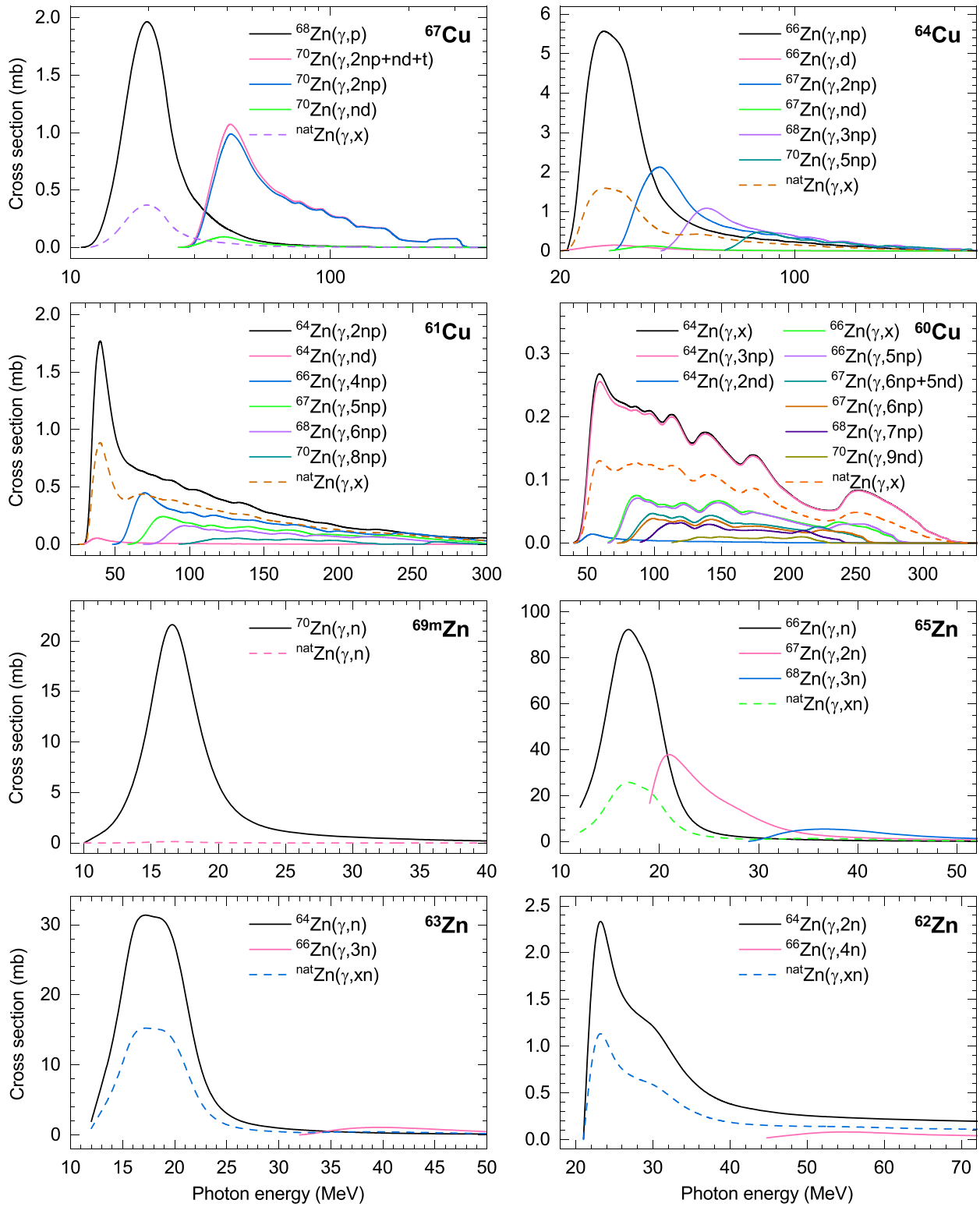

FIG. 8. Theoretical photonuclear reaction cross sections calculated by Eq. (4) in TALYS with default parameters for radionuclides produced alongside ^{67}Cu in the ^{nat}Zn(γ,x) reactions. The energy ranges selected for each reaction channel correspond to regions where the cross section is significant, highlighting their contributions to the overall production in a natural zinc target.

either short-lived, decaying rapidly during processing, or are isotopes of zinc that can be removed chemically. The production of ^{64}Cu in natural zinc arises mainly from the ^{66}Zn(γ,np) channel, which exhibits a maximum cross section of about 5.5 mb near 27 MeV, combined with the 27.73% natural abundance of ^{66}Zn. A secondary contribution arises from

TABLE V. Summary of ^{nat}Zn(γ,x) reaction products and their measured yields, averaged over three irradiation experiments.

Nuclide	Half-life	Yield (MBq μA^{-1}h^{-1}g^{-1})
^{67}Cu	61.83 h	0.410(16)
^{64}Cu	12.700 h	1.02(17)
^{61}Cu	3.339 h	0.419(29)
^{60}Cu	23.7 min	0.065(5)
^{69m}Zn	13.756 h	0.018(1)
^{65}Zn	243.93 d	5.71(35)
^{63}Zn	38.47 min	4.27(27)
^{62}Zn	9.193 h	0.280(13)

^{68}Zn(γ,3np), which opens at 36 MeV, and from ^{67}Zn(γ,2np), which opens at 26 MeV. At the endpoint energy of 855 MeV used in this work, all three channels are active, and the presence of ^{68}Zn and ^{67}Zn in the natural target further enhances the ^{64}Cu yield.

The situation changes fundamentally when enriched ^{68}Zn is employed. In that case, ^{64}Cu production is governed by the ^{68}Zn(γ,3np) path alone. A facility operating at energies below about 50 MeV (effectively below the 36 MeV threshold once the rapidly falling bremsstrahlung flux is considered) will suppress this channel. Under such conditions, ^{68}Zn(γ, p) dominates, producing ^{67}Cu with negligible contamination from ^{64}Cu. This explains why the ^{64}Cu / ^{67}Cu ratio achieved by photonuclear production on enriched ^{68}Zn is several orders of magnitude lower than in proton-induced routes, as shown in Table II. The contrast is most striking when compared to proton reactions. In the case of ^{68}Zn(p,2p)^{67}Cu, the competing ^{68}Zn(p,$n\alpha$)^{64}Cu channel opens at 8 MeV with a large maximum cross section of 23 mb at 28 MeV [20], far exceeding the nearly constant 10 mb cross section of the ^{68}Zn(p,2p)^{67}Cu channel above 40 MeV [62]. This imbalance leads to ^{64}Cu / ^{67}Cu ratios that are dramatically higher than those in photonuclear production, even when high-energy operation is used to moderate the effect. Although the ratio can be somewhat reduced at elevated energies, the onset of the ^{68}Zn(p,3n2p)^{64}Cu channel around 40 MeV prevents a decisive improvement [18]. In contrast, the ^{70}Zn(p,α)^{67}Cu reaction offers very favorable selectivity, since its competing ^{70}Zn(p,3$n\alpha$)^{64}Cu channel only opens at 24 MeV. With a 97.5% enriched ^{70}Zn target and operation at 17 MeV, where the desired channel peaks with a cross section of about 15 mb, ^{64}Cu contamination can be suppressed to below 0.003% [36]. Taken together, the excitation functions in Fig. 8 explain the spectral behavior observed experimentally and account for the observed ^{64}Cu yield, showing the clear advantage of photonuclear production on enriched ^{68}Zn in minimizing contamination.

A summary of all the reaction products, along with their respective measured yields, is provided in Table V. These yields represent the average values from three separate irradiation experiments, each carried out with varying irradiation times and target thicknesses. The averaging process also incorporated data from different gamma energy peaks of the same product, such as the 93.3 and 184.5 keV peaks for ^{67}Cu, used to calculate its yield.

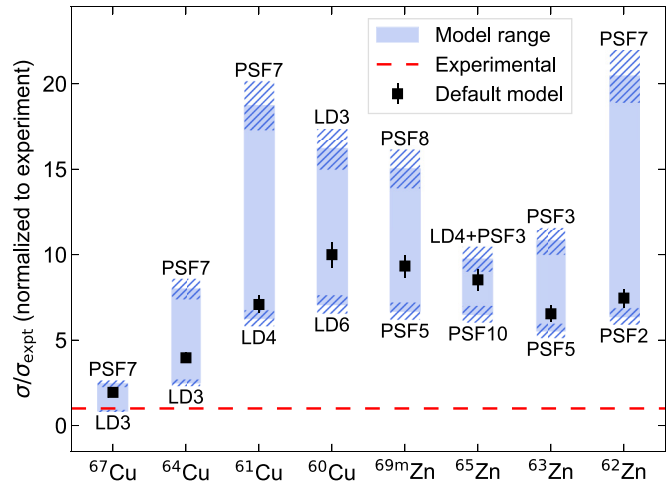

FIG. 9. Spectrum-weighted average cross sections predicted by TALYS (normalized to experimental values) plotted for each reaction product from ^{nat}Zn(γ,x) photonuclear reactions (x axis). The horizontal dashed line at 1.0 indicates the experimentally measured average cross section for each reaction, serving as a reference. Blue shaded bands represent the range of theoretical predictions obtained using different combinations of LD and PSF models in TALYS, with the upper and lower bounds corresponding to the maximum and minimum values, respectively. Black square markers indicate results from the TALYS default model. Labels above and below each band identify the specific model combinations yielding the maximum and minimum cross section values. Model configurations are detailed in Table VII and the numerical values are summarized in Table VI.

From these measured yields and the extended experimental bremsstrahlung spectrum, average cross sections were derived for each radionuclide and compared with theoretical values calculated using TALYS. Table VI summarizes these comparisons, showing the experimental values alongside the TALYS predictions using the default model configuration, as well as the minimum and maximum values obtained from a wide range of level density (LD) and PSF model combinations. These model variants are detailed in Table VII, with LD and PSF configurations labeled LD1–LD6 and PSF1–PSF10, respectively. The default predictions already exhibit substantial overestimation for most neutron-emission channels, often by factors of 6 or more, while the full model range illustrates the extent to which different theoretical assumptions influence the results. A visual representation of the same data is provided in Fig. 9, which highlights the systematic overprediction and the spread of theoretical results across different model configurations for each reaction product. This spread is further analyzed in the model sensitivity analysis sections below.

A. Model sensitivity analysis

To investigate the disagreement between measured and predicted cross sections, where TALYS reproduces (γ,p) channels but overestimates all (γ,xn) channels by factors of 6–10, we evaluated the sensitivity of TALYS calculations to key

TABLE VI. Spectrum-weighted average cross sections $\langle\sigma\rangle$ for ^{nat}Zn(γ,x) and selected enriched target reaction channels induced by bremsstrahlung photons with an endpoint energy of 855 MeV. Experimental values are compared with TALYS predictions using the default model (LD1+PSF9), and the lowest and highest results obtained from all LD and PSF combinations tested (see Table VII).

		$\langle\sigma\rangle_{theo}$				
			Minimum prediction		Maximum prediction	
Reaction	$\langle\sigma\rangle_{expt}$ (μb)	Default (μb)	Value (μb)	Model	Value (μb)	Model
^{68}Zn(γ, p) ^{67}Cu	150(6)	281(21)	127(10)	LD3	357(27)	PSF7
^{nat}Zn(γ, x) ^{67}Cu	28(1)	54(4)	24(2)	LD3	68(5)	PSF7
^{nat}Zn(γ, x) ^{64}Cu	84(14)	333(25)	210(16)	LD3	668(50)	PSF7
^{nat}Zn(γ, x) ^{61}Cu	38(3)	272(20)	240(18)	LD4	719(54)	PSF7
^{nat}Zn(γ, x) ^{60}Cu	7(1)	68(5)	48(4)	LD6	110(8)	LD3
^{70}Zn(γ, n)^{69m}Zn	197(17)	1817(136)	1396(105)	PSF5	2946(221)	PSF8
^{nat}Zn(γ, x) ^{69m}Zn	1.2(1)	11(1)	8(1)	PSF5	18(1)	PSF8
^{nat}Zn(γ, x) ^{65}Zn	369(26)	3146(236)	2393(180)	PSF10	3574(268)	LD4+PSF3
^{nat}Zn(γ, x) ^{63}Zn	304(21)	1988(149)	1676(126)	PSF5	3270(245)	PSF3
^{nat}Zn(γ, x) ^{62}Zn	24(1)	176(13)	150(11)	PSF2	482(36)	PSF7

nuclear inputs, especially LD and PSF models. Table VII summarizes the LD and PSF models tested within TALYS. These include the default configuration (LD1+PSF9), a range of widely used phenomenological and microscopic models, as well as temperature-dependent extensions. Figures 10–17 present the calculated cross sections for each reaction using various LD and PSF combinations, highlighting the substantial spread introduced by different nuclear input models. The following subsections dissect each component (preequilibrium, LD, PSF, etc.) to clarify which theoretical assumptions drive the neutron-emission overpredictions.

1. Preequilibrium and high-excitation effects

TALYS incorporates a multistep exciton model for preequilibrium emission (using numerical transition rates) alongside the standard Hauser–Feshbach compound nucleus model. While this framework can describe particle emission at moderately high energies, it is based on statistical assumptions that may break down at the extreme excitation energies induced by bremsstrahlung photons at endpoint energies such as 855 MeV. At such energies, the nucleus is excited well beyond the range for which TALYS has been benchmarked, and the preequilibrium model may not fully capture the complexity of reaction dynamics. Rather than evolving smoothly from preequilibrium to compound nucleus formation, the system may favor direct or prompt particle emission mechanisms, including multiparticle knockout. As a result, the exciton model may misrepresent the competition between neutron and proton emission channels and overestimate the probability of neutron evaporation. This can lead to inflated reaction rates, as previously reported [81].

TABLE VII. Level density (LD) and photon strength function (PSF) models used in TALYS calculations. These are referenced in figures as LD1–LD6 and PSF1–PSF10. LD1 and PSF9 correspond to TALYS default models. When only PSF models are varied, LD1 is used; when only LD models are varied, PSF9 is used. Combined LD-PSF configurations are indicated where explicitly used.

Label	Model type	Description	Reference
LD1	Constant temperature + Fermi gas (CTM)	TALYS default LD model	[63,64]
LD2	Back-shifted Fermi gas (BFM)	Phenomenological model with energy shift	[65]
LD3	Generalized superfluid (GSM)	Empirical model with pairing correlations	[66,67]
LD4	Skyrme-Hartree-Fock-Bogoliubov (HFB) tables	Microscopic LD from Skyrme HFB calculations	[68]
LD5	Skyrme HFB combinatorial tables	Combinatorial LD from HFB single-particle states	[69]
LD6	Gogny-HFB T-dependent combinatorial tables	Temperature-dependent Gogny HFB level densities	[70]
PSF1	Kopecky-Uhl generalized Lorentzian	Empirical Lorentzian with temperature effects	[71]
PSF2	Brink-Axel Lorentzian	Standard $E1$ strength with fixed width	[72,73]
PSF3	Skyrme-Hartree-Fock + BCS (HF+BCS) tables	Microscopic PSF based on HF+BCS theory with QRPA	[74]
PSF4	Skyrme-Hartree-Fock-Bogoliubov (HFB) tables	Microscopic PSF from HFB calculations	[75]
PSF5	Goriely's hybrid model	Empirical–microscopic hybrid PSF model	[76]
PSF6	T-dependent Goriely HFB	Temperature-dependent extension of PSF4	[75]
PSF7	T-dependent relativistic mean field (RMF)	Microscopic PSF from RMF calculations	[77]
PSF8	Gogny D1M HFB+QRPA	Microscopic PSF from Gogny HFB+QRPA calculations	[78]
PSF9	Simplified modified Lorentzian (SMLO)	Phenomenological model; TALYS default PSF	[79,80]
PSF10	Skyrme HFB+QRPA	Microscopic PSF from Skyrme HFB+QRPA calculations	[75]

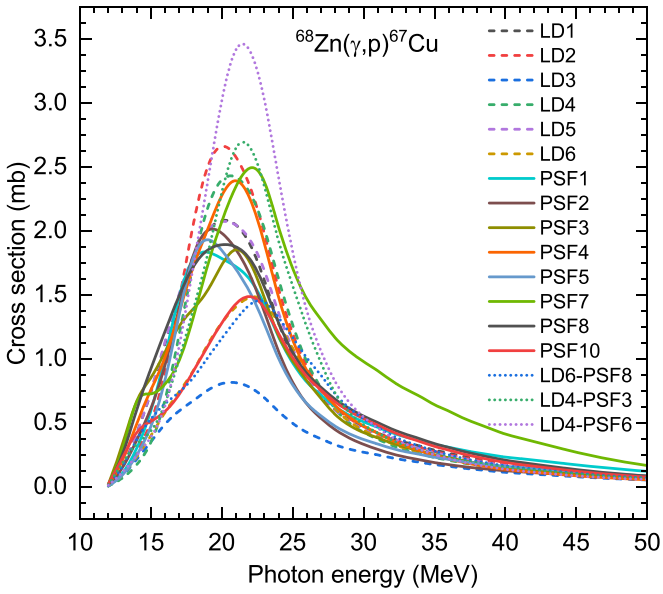

FIG. 10. Theoretical cross sections for the ^{68}Zn(γ, p)^{67}Cu reaction calculated using TALYS with various combinations of LD and PSF models. Model labels (LD1–LD6 and PSF1–PSF10) correspond to those defined in Table VII. Exploring alternative TALYS model inputs provides insight into the degree to which nuclear input choices contribute to the observed experimental-theoretical discrepancy.

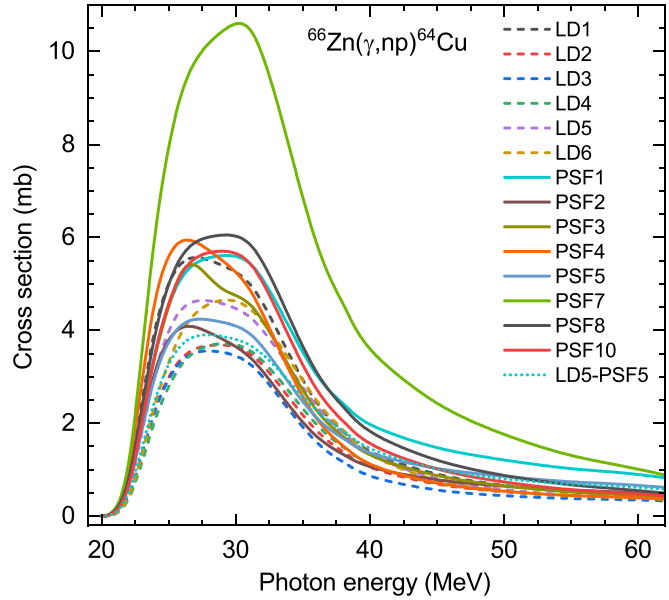

FIG. 11. Same as Fig. 10, but for the ^{66}Zn(γ,np)^{64}Cu reaction.

In the present calculations, the default exciton model and the constant temperature plus Fermi gas model (CTM) for LD were employed. However, these models are not specifically tuned for zinc isotopes. If the assumed LD is too high at large excitation energies, the number of open decay channels, particularly those involving neutron emission, can be overpredicted, further contributing to the overestimation of (γ, xn) yields.

2. Level density behavior

At very high compound excitation energies, the nucleus has access to extremely high LDs. TALYS employs global LD parametrizations such as the CTM, back-shifted Fermi gas model (BFM), generalized superfluid model (GSM), and various microscopic Hartree-Fock-Bogoliubov (HFB) approaches. These are mostly fitted near particle thresholds, not for the hundreds of MeV reached in bremsstrahlung activation. If these models overestimate the LD at high excitation energies, statistical decay is biased towards multiparticle emissions. Without experimental photoneutron data for Zn at these energies, the LD parameters remain unconstrained.

As shown in Figs. 10–17, different LD models yield varied broadening, peak cross sections, and spectral tails. For example, the HFB models (LD4–LD6) result in broader high-energy tails.

3. Photon interactions beyond the GDR

The GDR in Zn isotopes lies around 15–20 MeV. In this range, $E1$ photon absorption dominates and TALYS's Lorentzian GDR models are reasonably constrained. In fact, TALYS uses the only available experimental GDR parameters for ^{64}Zn [82] within the simplified modified Lorentzian (SMLO) framework: a two-humped GDR characterized by resonance strengths $\sigma_1 = 48.04$ mb and $\sigma_2 = 47.80$ mb, resonance energies $E_1 = 16.37$ MeV and $E_2 = 19.49$ MeV, and widths $\Gamma_1 = 3.84$ MeV and $\Gamma_2 = 5.82$ MeV. Above the GDR, the QD mechanism governs the falloff of the photoabsorption tail. This QD contribution is therefore present in all calculations used here and is an essential ingredient of the folded cross sections.

The key limitation for our endpoint energies is the treatment above the meson production region. Although TALYS outputs cross sections up to 1 GeV, it does so by a

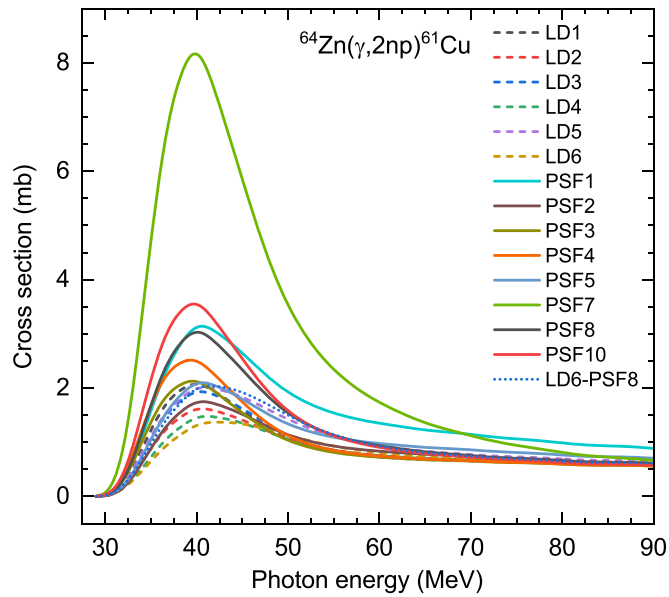

FIG. 12. Same as Fig. 10, but for the ^{64}Zn(γ,$2np$)^{61}Cu reaction.

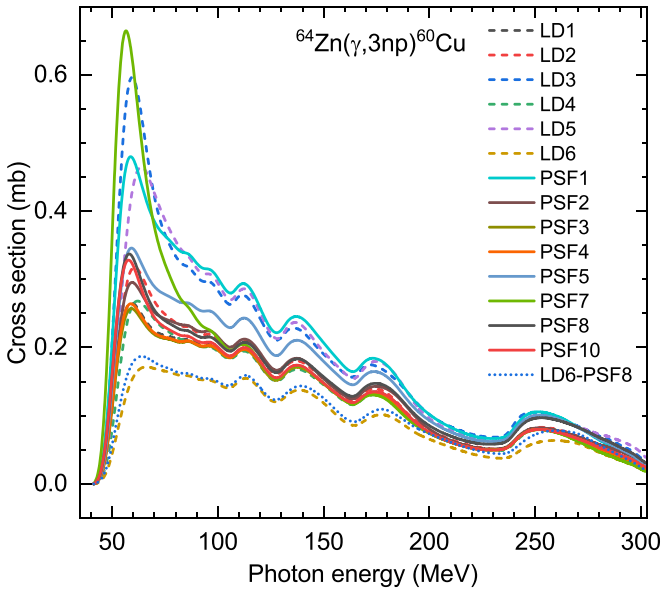

FIG. 13. Same as Fig. 10, but for the ^{64}Zn(γ,3np)^{60}Cu reaction.

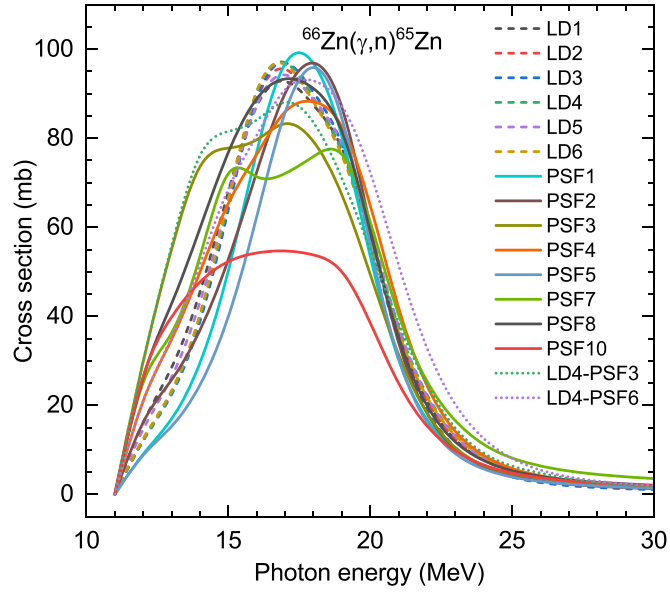

FIG. 15. Same as Fig. 10, but for the ^{66}Zn(γ,n)^{65}Zn reaction.

simple empirical continuation of the optical model picture beyond $\approx$ 200 MeV [83]; explicit pion production and nucleon-resonance dynamics are not included. In practice this produces a smoothly decreasing extension of the QD strength with a small, nonphysical break in the slope around the pion threshold, and it misallocates high-energy photon-absorption strength into nucleon-evaporation channels. Under a bremsstrahlung spectrum, that misallocation inflates the spectrum-weighted (γ,xn) cross sections.

Physically, once $E_\gamma \gtrsim 140$ MeV, the interaction proceeds largely on individual nucleons: first through excitation of the $\Delta(1232)$ resonance (centered near 300 MeV), and then via higher N^* states at increasing energy. These resonances decay predominantly with pion emission, feeding intranuclear cascades that redistribute strength among meson, nucleon, and multinucleon channels rather than simple neutron evaporation. The dominant contribution is from incoherent pion production, which includes charged pions, $\pi^\pm$, and neutral pions, π^0, where the residual nucleus is left in an excited or fragmented state. For heavy nuclei, a substantial additional component arises from coherent π^0 photoproduction, in which the photon couples to the entire nuclear ground state; this channel scales approximately as A^2 and, in the Δ region, reaches peak total cross sections of about 2.4 mb for ^{208}Pb, 0.85 mb for ^{40}Ca, and 0.6 mb for ^{18}O [84,85]. Fits to differential cross sections also require a small incoherent

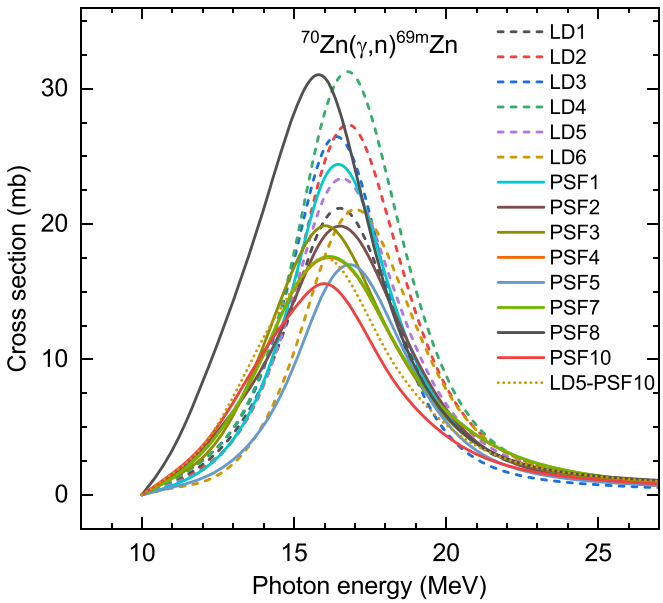

FIG. 14. Same as Fig. 10, but for the ^{70}Zn(γ,n)^{69m}Zn reaction.

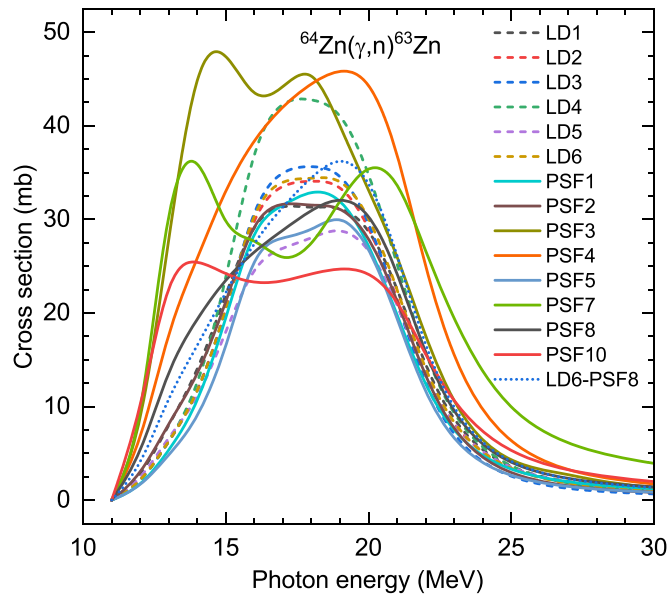

FIG. 16. Same as Fig. 10, but for the ^{64}Zn(γ,n)^{63}Zn reaction.

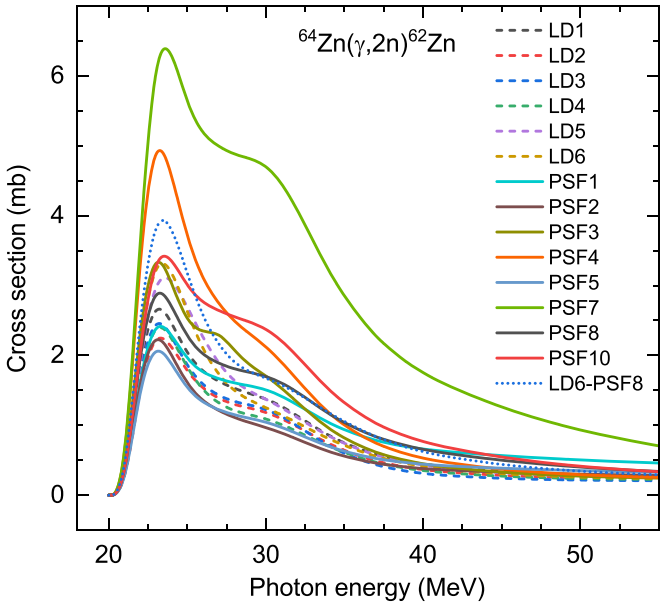

FIG. 17. Same as Fig. 10, but for the ^{64}Zn(γ,2n)^{62}Zn reaction.

π^0 fraction, typically a few percent of the coherent yield for heavy targets. Higher-lying resonances have much lower contributions to coherent and incoherent channels. None of these mechanisms are represented in TALYS, so their strength is effectively reassigned to nucleon-evaporation cascades in the model. A well-established empirical feature is that the *per-nucleon* total photoabsorption in the Δ region is approximately A independent from light to heavy nuclei within uncertainties; nuclear-medium effects (Fermi motion smearing, Pauli blocking, and in-medium propagation/coupling of the Δ to NN and other channels) modestly broaden and slightly suppress the peak relative to the free proton but do not change the overall scale [86]. This approximate A scaling underpins our use of published heavy- and medium-mass data as a proxy for Zn in the resonance region. Figure 18 leverages that proxy: it overlays our TALYS total photoabsorption for all Zn isotopes and ^{nat}Zn (to 1 GeV) with experimental total photoabsorption data from Refs. [87,88], normalized to natural Zn for direct comparison. The normalized data exhibit the expected resonance enhancement above $\approx$ 140 MeV through the Δ region and beyond, whereas the TALYS curves contain only the GDR plus QD continuation and stay low and nearly featureless at high energy. This mismatch is precisely the missing pion/resonance physics: TALYS underestimates the total absorption in the resonance domain but simultaneously channels its high-energy strength into evaporation, biasing the spectrum-weighted (γ,xn) yields upward. This behavior likely contributes to the observed discrepancy pattern, where TALYS tends to fare worse for multineutron channels, which are more sensitive to the missing pion-nucleon cascade strength, than for proton channels, which are comparatively more constrained by the Coulomb barrier and by low-energy absorption.

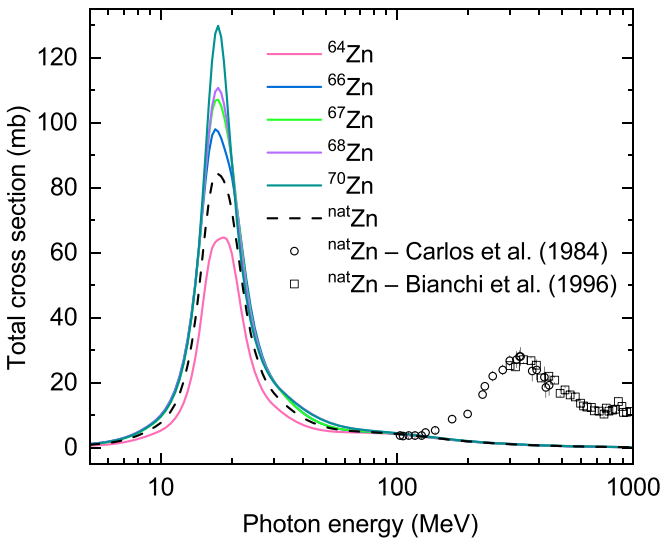

FIG. 18. Total photoabsorption cross sections for individual Zn isotopes and natural Zn calculated with TALYS up to 1 GeV, compared with experimental Pb data from [88] and [87], normalized to natural Zn for direct comparison.

4. Photon strength function sensitivity

The PSF is a critical nuclear input in nuclear model codes that governs the shape and magnitude of the photoabsorption cross section. TALYS offers several phenomenological and microscopic PSFs. The default (PSF9) is the SMLO. Our model sensitivity analysis indicates that PSF choice significantly alters the predicted cross sections. For instance, changing PSF9 to PSF7 (a temperature-dependent relativistic mean-field model) for ^{nat}Zn(γ, x)^{61}Cu and ^{62}Zn increases the cross section by up to a factor of 2.7. This is due to changes in resonance width, centroid, and tail behavior. As the experimental bremsstrahlung extends far above the GDR, PSF differences at high E_γ substantially affect spectrum-weighted results.

Microscopic PSFs often produce broader or higher-energy-shifted resonances, increasing overlap with the bremsstrahlung tail. These effects are evident in the cross section variations plotted in Figs. 10–17. Without detailed Zn photoabsorption data above the GDR, these models are poorly constrained and contribute to the overestimation.

5. Spectrum-weighted averaging and spectral bias

In this analysis, the experimental spectrum-weighted cross sections $\langle\sigma\rangle_{\rm expt}$, obtained over the effective energy range from the respective reaction thresholds up to 855 MeV, are compared with theoretical values $\langle\sigma\rangle_{\rm theo}$ calculated over the same interval. The bremsstrahlung spectrum is strongly peaked at low energies but features a long high-energy tail. Consequently, any nonzero predicted cross section beyond the GDR region contributes to the average. If the model overestimates $\sigma(E)$ in this high-energy regime, the resulting $\langle\sigma\rangle_{\rm theo}$ becomes inflated. Even a moderate overprediction of $\sigma(\gamma,xn)$ at several hundred MeV can significantly affect the spectrum-weighted result, exacerbating the discrepancy between experiment and theory. This highlights the importance of evaluating theoretical calculations across the full bremsstrahlung spectrum, rather than focusing solely on the GDR peak.

6. (γ, p) versus neutron channel behavior

Both (γ,n) and (γ,p) reactions exhibit strength concentrated in the GDR region, as reflected in the shape of their excitation functions. However, the (γ,p) channel tends to be more localized due to the presence of the Coulomb barrier, which restricts the emission of protons at low excitation energy and limits the effective width of the channel. This energy filtering reduces the contribution from the high-energy tail of the bremsstrahlung spectrum, making (γ,p) reactions less sensitive to uncertainties in the model input at high photon energies. As a result, TALYS predictions for the (γ,p) cross section show better agreement with experimental data.

In contrast, neutron emission is not constrained by a Coulomb barrier and can occur over a broader range of excitation energies. Multineutron emission channels, such as (γ,2n) and (γ,xn), extend well above the GDR and into regions where QD and preequilibrium mechanisms dominate. TALYS's LD and PSF models are less constrained in these regions, and any overestimation is amplified by the contribution from the high-energy bremsstrahlung spectrum. This leads to a systematic overprediction of (γ,xn) yields, particularly for higher-multiplicity neutron channels.

7. Potential model improvements

The observed overestimation in neutron-emission cross sections reflects compounded sensitivities across multiple theoretical components rather than a single model failure. While TALYS offers a flexible and comprehensive framework, providing access to numerous LD, PSF, and other models and parameters, the continuous nature of bremsstrahlung activation complicates source attribution. Unlike monoenergetic beam studies, which can isolate energy-dependent discrepancies, spectrum-weighted experiments integrate contributions from a broad range of excitation energies, where different reaction mechanisms dominate.

Potential improvements include refining the PSF to better represent high-energy photoabsorption in Zn isotopes, possibly by adopting updated systematics or incorporating experimental GDR data beyond the SMLO defaults. LD models could be adjusted using combinatorial or resonance-calibrated approaches tailored to Zn, especially to constrain behavior at high excitation energy. The preequilibrium emission model may benefit from more detailed energy-dependent tuning, or inclusion of extended reaction channels such as (γ,xnp), to better partition emission strength in the multi-particle domain. For photon energies above 200 MeV, improved treatment of QD absorption and the introduction of direct or pion-related mechanisms may help address limitations in current high-energy extrapolations.

While we did not attempt to retune parameters for *post hoc* agreement, the modularity of the theoretical code would allow such refinements. However, the folded nature of the bremsstrahlung-based activation data complicates definitive interpretation. Without energy-resolved information, it is difficult to pinpoint whether discrepancies arise primarily from threshold effects, resonance mismodeling, or reaction-channel misattribution. To resolve this, future experiments employing monoenergetic or finely tagged photon beams are essential. Such measurements would allow exclusive reaction channels to be isolated and benchmarked against theory at specific energies, disentangling contributions from GDR, preequilibrium, and QD regimes. These studies are not only crucial for improving predictive power in applied contexts such as isotope production, but also carry significant implications for the broader field of nuclear reaction modeling and nucleosynthesis calculations.

B. Photonuclear yield and scalability of ^{67}Cu production

A key aim of this work was to assess the feasibility of using high-energy bremsstrahlung photons for the production of the theranostic isotope ^{67}Cu. The measured yield of ^{67}Cu in this study was 0.410(16) MBq μA^{-1}h^{-1}g^{-1}, demonstrating the viability of the 855 MeV bremsstrahlung approach for isotope production. This value compares favorably with reported yields from lower-energy bremsstrahlung setups. For example, yields of 0.1517, 0.2863, 0.3411, and 0.4773 MBq μA^{-1}h^{-1}g^{-1} were reported in Ref. [31] for electron endpoint energies of 30, 40, 50, and 60 MeV, respectively. Another study at 40 MeV [39] reported a yield of 0.176 MBq μA^{-1}h^{-1}g^{-1}. These comparisons indicate that high-energy bremsstrahlung can be a viable route for ^{67}Cu production, with scope for further optimization.

The ^{68}Zn(γ, p)^{67}Cu reaction is scalable with respect to beam current and irradiation time, provided that thermal management and radiation shielding are adequately addressed. Increasing the target mass offers another route to higher yields; however, the effective thickness is constrained by the radiation length of Zn, beyond which attenuation of bremsstrahlung photons reduces the usable flux.

Lower-energy electron linacs (<50 MeV) provide another pathway for isotope generation, offering finer control over excitation energy and potentially reducing the formation of unwanted byproducts. Their relatively compact size and modest shielding requirements make them suitable for decentralized or hospital-based facilities. At the other end of the spectrum, high-current, high-duty-cycle facilities, such as JLab, present opportunities for parasitic isotope harvesting. Existing infrastructure and extended operational cycles at such facilities can be leveraged to recover radioisotopes from beam dumps without disrupting core experimental activities. Ongoing advances in accelerator technologies may further improve the accessibility of ^{67}Cu production. Compact laser-plasma accelerators [89] have demonstrated promising beam parameters in the 15–250 MeV range [90–92], with continuing efforts focused on improving beam quality, energy spread, and repetition rates. While such parameters are beneficial, it is primarily the achievable integral photon flux in the vicinity of the GDR region that governs the suitability of these sources for photoproduction applications. In parallel, high-power superconducting linacs are being developed specifically for large-scale radioisotope production [93]. While not compact, these systems may support regional distribution models and complement emerging decentralized production schemes.

Continued progress in photonuclear production will benefit from an integrated approach, combining improved nuclear modeling with practical developments in accelerator

systems, target engineering, and post-irradiation radiochemical workflows.

IV. CONCLUSIONS

This study demonstrates the feasibility of producing ^{67}Cu through bremsstrahlung-induced photonuclear reactions at high-energy electron accelerators. A yield of 0.410(16) MBq $\mu A^{-1} h^{-1} g^{-1}$ was obtained using an 855 MeV beam, representing one of the highest reported for this route. When paired with enriched ^{68}Zn targets, this route offers good scalability and competitive specific activity.

Theoretical predictions from TALYS, although consistent with experimental data for proton-emission channels, significantly overestimate neutron-emission and multiparticle channel cross sections. This discrepancy arises from the cumulative effects of LD, PSF, and preequilibrium emission models, particularly in the high-excitation energy regime accessed by bremsstrahlung activation. These findings highlight the need for more constrained nuclear inputs and improved modeling of photonuclear reactions at high energies.

From a practical standpoint, bremsstrahlung-based ^{67}Cu production offers several advantages. Electron beams are cost-effective to generate, and low-energy linacs are compact and relatively easy to shield, making them well suited for decentralized production facilities. At the same time, high-current accelerator centers, including facilities originally built for fundamental physics, may enable parasitic isotope production using existing infrastructure. These options complement emerging laser-plasma accelerator and superconducting linac technologies, which promise more compact, high-flux electron sources.

Altogether, photonuclear methods, when combined with optimized targetry and radiochemical workflows, represent a sustainable alternative to reactor-based production of therapeutic isotopes such as ^{177}Lu. With further development, these techniques could help address ongoing supply challenges and broaden access to key radiotheranostic isotopes like ^{67}Cu.

ACKNOWLEDGMENTS

We thank the MAMI facility and the A2 Collaboration at Johannes Gutenberg University Mainz (JGU) for making it possible to carry out the experiment. We also thank Jürgen Diefenbach and Oleksandr Kostikov of JGU for their technical help, and we are grateful for the travel support provided through Transnational access to European Research Infrastructures. We also thank the anonymous referee for helpful comments that improved this paper. This work was supported by the UK Science and Technology Facilities Council (STFC) Grant No. ST/V001035/1.

DATA AVAILABILITY

The data that support the findings of this article are not publicly available upon publication because it is not technically feasible and/or the cost of preparing, depositing, and hosting the data would be prohibitive within the terms of this research project. The data are available from the authors upon reasonable request.

[1] S. Del Vecchio, A. Zannetti, R. Fonti, L. Pace, and M. Salvatore, Q. J. Nucl. Med. Mol. Imaging **51**, 152 (2007).
[2] F. Rösch, H. Herzog, and S. M. Qaim, Pharmaceuticals **10**, 56 (2017).
[3] E. W. Price and C. Orvig, Chem. Soc. Rev. **43**, 260 (2014).
[4] A. G. Follacchio, S. M. De Feo, G. De Vincentis, F. Monteleone, and M. Liberatore, Curr. Radiopharm. **11**, 22 (2018).
[5] G. Ting, C.-H. Chang, and H.-E. Wang, Anticancer Res. **29**, 4107 (2009).
[6] P. A. Schubiger, R. Alberto, and A. Smith, Bioconjugate Chem. **7**, 165 (1996).
[7] Y. Sugo, K. Hashimoto, M. Kawabata, H. Saeki, S. Sato, K. Tsukada, and Y. Nagai, J. Phys. Soc. Jpn. **86**, 023201 (2017).
[8] K. Zimmermann, J. Grünberg, M. Honer, S. Ametamey, P. August Schubiger, and I. Novak-Hofer, Nucl. Med. Biol. **30**, 417 (2003).
[9] H. Junde, H. Xiaolong, and J. Tuli, Nucl. Data Sheets **106**, 159 (2005).
[10] A. Boschi, P. Martini, E. Janevik-Ivanovska, and A. Duatti, Drug Discov. Today **23**, 1489 (2018).
[11] F. Peng, X. Lu, J. Janisse, O. Muzik, and A. F. Shields, J. Nucl. Med. **47**, 1649 (2006).
[12] Z.-H. Jin *et al.*, Nucl. Med. Commun. **38**, 347 (2017).
[13] B. M. Katz and A. Barnea, J. Biol. Chem. **265**, 2017 (1990).
[14] K. Knogler, J. Grünberg, K. Zimmermann, S. Cohrs, M. Honer, S. Ametamey, P. Altevogt, M. Fogel, P. A. Schubiger, and I. Novak-Hofer, Clin. Cancer Res. **13**, 603 (2007).
[15] I. Novak-Hofer and A. P. Schubiger, Eur. J. Nucl. Med. Mol. Imaging **29**, 821 (2002).
[16] N. A. Smith, D. L. Bowers, and D. A. Ehst, Appl. Radiat. Isot. **70**, 2377 (2012).
[17] T. Katabuchi, S. Watanabe, N. S. Ishioka, Y. Iida, H. Hanaoka, K. Endo, and S. Matsuhashi, J. Radiol. Nucl. Chem. **277**, 467 (2008).
[18] D. G. Medvedev, L. F. Mausner, G. E. Meinken, S. O. Kurczak, H. Schnakenberg, C. J. Dodge, E. M. Korach, and S. C. Srivastava, Appl. Radiat. Isot. **70**, 423 (2012).
[19] D. J. sr Jamriska, W. A. Taylor, M. A. Ott, R. C. Heaton, D. R. Phillips, and M. M. Fowler, J. Radiol. Nucl. Chem. **195**, 263 (1995).
[20] K. Hilgers, T. Stoll, Y. Skakun, H. Coenen, and S. Qaim, Appl. Radiat. Isot. **59**, 343 (2003).
[21] J. Kozempel, K. Abbas, F. Simonelli, A. Bulgheroni, U. Holzwarth, and N. Gibson, Radiochim. Acta **100**, 419 (2012).
[22] T. Ohya, K. Nagatsu, H. Suzuki, M. Fukada, K. Minegishi, M. Hanyu, and M.-R. Zhang, Nucl. Med. Biol. **59**, 56 (2018).
[23] Y. Skakun and S. Qaim, Appl. Radiat. Isot. **60**, 33 (2004).
[24] M. Kawabata, K. Hashimoto, H. Saeki, N. Sato, S. Motoishi, K. Takakura, C. Konno, and Y. Nagai, J. Radiol. Nucl. Chem. **303**, 1205 (2015).
[25] T. Kin *et al.*, J. Phys. Soc. Jpn. **82**, 034201 (2013).
[26] N. Sato *et al.*, J. Phys. Soc. Jpn. **83**, 073201 (2014).
[27] I. Spahn, H. H. Coenen, and S. M. Qaim, Radiochim. Acta **92**, 183 (2004).

[28] A. Gopalakrishna *et al.*, Radiochim. Acta **106**, 549 (2018).
[29] V. N. Starovoitova, L. Tchelidze, and D. P. Wells, Appl. Radiat. Isot. **85**, 39 (2014).
[30] V. N. Starovoitova, P. L. Cole, and T. L. Grimm, J. Radiol. Nucl. Chem. **305**, 127 (2015).
[31] M. Yagi and K. Kondo, Int. J. Appl. Radiat. Isot. **29**, 757 (1978).
[32] A. Koning, S. Hilaire, and S. Goriely, Eur. Phys. J. A **59**, 131 (2023).
[33] R. Schwarzbach, K. Zimmermann, P. Bläuenstein, A. Smith, and P. August Schubiger, Appl. Radiat. Isot. **46**, 329 (1995).
[34] A. Dasgupta, L. Mausner, and S. Srivastava, Int. J. Radiat. Appl. Instrum. A **42**, 371 (1991).
[35] S. Mirzadeh, L. Mausner, and S. Srivastava, Int. J. Radiat. Appl. Instrum. A **37**, 29 (1986).
[36] S. A. Brühlmann, M. Walther, M. Kreller, F. Reissig, H.-J. Pietzsch, T. Kniess, and K. Kopka, Pharmaceuticals **16**, 314 (2023).
[37] M. J. Merrick, D. A. Rotsch, A. Tiwari, J. Nolen, T. Brossard, J. Song, T. J. Wadas, J. J. Sunderland, and S. A. Graves, Phys. Med. Biol. **66**, 035002 (2021).
[38] N. Marceau, T. Kruck, D. McConnell, and N. Aspin, Int. J. Appl. Radiat. Isot. **21**, 667 (1970).
[39] G. Hovhannisyan, T. Bakhshiyan, and R. Dallakyan, Nucl. Instrum. Methods Phys. Res. Sect. B **498**, 48 (2021).
[40] N. I. Aizatsky, N. P. Diky, A. N. Dovbnya, D. Ehst, Yu. V. Lyashko, V. I. Nikiforov, A. Eh. Tenishev, A. V. Torgovkin, V. L. Uvarov, V. A. Shevchenko, and B. I. Shramenko, Probl. At. Sci. Technol. **53**, 140 (2010).
[41] V. Starovoitova, D. Foote, J. Harris, V. Makarashvili, C. R. Segebade, V. Sinha, and D. P. Wells, AIP Conf. Proc. **1336**, 502 (2011).
[42] M. Kawabata, S. Motoishi, A. Ohta, A. Motomura, H. Saeki, K. Tsukada, S. Hashimoto, N. Iwamoto, Y. Nagai, and K. Hashimoto, J. Radiol. Nucl. Chem. **330**, 913 (2021).
[43] H. Herminghaus, A. Feder, K. Kaiser, W. Manz, and H. Schmitt, Nucl. Instrum. Methods **138**, 1 (1976).
[44] A2 Collaboration, official website, https://wwwa2.kph.uni-mainz.de/.
[45] E. Mornacchi, Measurement of the proton scalar polarizabilities at MAMI, Ph.D. thesis, Johannes Gutenberg-Universität Mainz, (2021), https://doi.org/10.25358/openscience-6051.
[46] J. Allison *et al.*, Nucl. Instrum. Methods Phys. Res. Sect. A **835**, 186 (2016).
[47] S. T. Perkins, D. E. Cullen, and S. M. Seltzer, Tables and graphs of electron-interaction cross sections from 10 eV to 100 GeV derived from the LLNL Evaluated Electron Data Library (EEDL), $Z = 1$–100, Lawrence Livermore National Laboratory Technical Report, 1991, https://doi.org/10.2172/5691165.
[48] V. Ivanchenko *et al.*, EPJ Web Conf. **245**, 02009 (2020).
[49] R. Brun, F. Bruyant, F. Carminati, S. Giani, M. Maire, A. McPherson, G. Patrick, and L. Urban, GEANT: Detector description and simulation tool, Oct. 1994, CERN Program Library, long writeup W5013, CERN, 1993, https://cds.cern.ch/record/1082634.
[50] Y.-S. Tsai, Rev. Mod. Phys. **46**, 815 (1974).
[51] NEA, PENELOPE 2018: A code system for Monte Carlo simulation of electron and photon transport: Workshop proceedings, Barcelona, OECD Publishing, Paris, Spain, 28 January – 1 February, 2019, https://doi.org/10.1787/32da5043-en.
[52] Zinc foil, Goodfellow online technical data sheet for product, https://www.goodfellow.com/uk/zinc-foil-1000225674.
[53] Calibration source, Eckert & Ziegler NG3 nuclide mixture calibration standard, https://www.ezag.com/products/isotope-products/isotrak-calibration-sources/reference-sources/geometry-sources/nuclide-mixtures-ng1-to-ng6/.
[54] J. Meija *et al.*, Pure Appl. Chem. **88**, 293 (2016).
[55] J. H. Hubbell and S. M. Seltzer, Tables of x-ray mass attenuation coefficients and mass energy-absorption coefficients (version 1.4), http://physics.nist.gov/xaamdi.
[56] M. B. Chadwick, P. Obložinský, P. E. Hodgson, and G. Reffo, Phys. Rev. C **44**, 814 (1991).
[57] R. Capote *et al.*, Nucl. Data Sheets **110**, 3107 (2009).
[58] J. S. Levinger, Phys. Rev. **84**, 43 (1951).
[59] J. R. Wu and C. C. Chang, Phys. Rev. C **16**, 1812 (1977).
[60] J. Levinger, Phys. Lett. B **82**, 181 (1979).
[61] L. A. Currie, Anal. Chem. **40**, 586 (1968).
[62] T. Stoll, S. Kastleiner, Y. N. Shubin, H. H. Coenen, and S. M. Qaim, Radiochim. Acta **90**, 309 (2002).
[63] T. Ericson, Adv. Phys. **9**, 425 (1960).
[64] A. Gilbert and A. G. W. Cameron, Can. J. Phys. **43**, 1446 (1965).
[65] W. Dilg, W. Schantl, H. Vonach, and M. Uhl, Nucl. Phys. A **217**, 269 (1973).
[66] A. V. Ignatyuk, K. K. Istekov, and G. N. Smirenkin, Sov. J. Nucl. Phys. **29**, 875 (1979).
[67] A. V. Ignatyuk, J. L. Weil, S. Raman, and S. Kahane, Phys. Rev. C **47**, 1504 (1993).
[68] S. Goriely, F. Tondeur, and J. Pearson, At. Data Nucl. Data Tables **77**, 311 (2001).
[69] S. Goriely, S. Hilaire, and A. J. Koning, Phys. Rev. C **78**, 064307 (2008).
[70] S. Hilaire, M. Girod, S. Goriely, and A. J. Koning, Phys. Rev. C **86**, 064317 (2012).
[71] J. Kopecky and M. Uhl, Phys. Rev. C **41**, 1941 (1990).
[72] D. Brink, Nucl. Phys. **4**, 215 (1957).
[73] P. Axel, Phys. Rev. **126**, 671 (1962).
[74] S. Goriely and E. Khan, Nucl. Phys. A **706**, 217 (2002).
[75] S. Goriely, E. Khan, and M. Samyn, Nucl. Phys. A **739**, 331 (2004).
[76] S. Goriely, Phys. Lett. B **436**, 10 (1998).
[77] I. Daoutidis and S. Goriely, Phys. Rev. C **86**, 034328 (2012).
[78] S. Goriely, S. Hilaire, S. Péru, and K. Sieja, Phys. Rev. C **98**, 014327 (2018).
[79] V. Plujko, O. Gorbachenko, R. Capote, and P. Dimitriou, At. Data Nucl. Data Tables **123-124**, 1 (2018).
[80] S. Goriely and V. Plujko, Phys. Rev. C **99**, 014303 (2019).
[81] S. Goriely, S. Hilaire, and A. J. Koning, Astron. Astrophys. **487**, 767 (2008).
[82] S. S. Dietrich and B. L. Berman, At. Data Nucl. Data Tables **38**, 199 (1988).
[83] A. Koning, D. Rochman, and S. van der Marck, Nucl. Data Sheets **118**, 187 (2014).
[84] C. M. Tarbert *et al.* (Crystal Ball at MAMI and A2 Collaboration), Phys. Rev. Lett. **112**, 242502 (2014).
[85] C. M. Tarbert, Coherent π^0 photoproduction on nuclei, Ph.D. thesis, University of Edinburgh, 2007, https://era.ed.ac.uk/handle/1842/3501.
[86] J. Ahrens, Nucl. Phys. A **446**, 229 (1985).
[87] N. Bianchi, V. Muccifora, E. De Sanctis, A. Fantoni, P. Levi Sandri, E. Polli, A. R. Reolon, P. Rossi, M. Anghinolfi, P. Corvisiero, M. Ripani, M. Sanzone, M. Taiuti, and A. Zucchiatti, Phys. Rev. C **54**, 1688 (1996).

[88] P. Carlos, H. Beil, R. Bergére, J. Fagot, A. Leprêtre, A. Demeniac, and A. Veyssiére, Nucl. Phys. A **431**, 573 (1984).
[89] T. Tajima and J. M. Dawson, Phys. Rev. Lett. **43**, 267 (1979).
[90] S. P. D. Mangles, C. D. Murphy, Z. Najmudin, A. G. R. Thomas, J. L. Collier, A. E. Dangor, E. J. Divall, P. S. Foster, J. G. Gallacher, C. J. Hooker, D. A. Jaroszynski, A. J. Langley, W. B. Mori, P. A. Norreys, F. S. Tsung, R. Viskup, B. R. Walton, and K. Krushelnick, Nature (London) **431**, 535 (2004).
[91] J. Faure, Y. Glinec, A. Pukhov, S. Kiselev, S. Gordienko, E. Lefebvre, J.-P. Rousseau, F. Burgy, and V. Malka, Nature (London) **431**, 541 (2004).
[92] J. Faure, C. Rechatin, A. Norlin, A. Lifschitz, Y. Glinec, and V. Malka, Nature (London) **444**, 737 (2006).
[93] J. Krämer, G. Blokesch, M. Grewe, B. Keune, V. Kümper, M. Pekeler, C. Piel, C. Quitmann, T. Trinh, and P. vom Stein, in *Proceedings of the 31st International Linear Accelerator Conference (LINAC'22)* (JACoW, Geneva, 2022), pp. 35–37.